Stability of Aerospace Thin-Walled Structures: Investigating Pre-Buckling and Post-Buckling Behaviors in Glass Laminate Aluminum Reinforced Epoxy (GLARE) C-Beams with Cross Stiffeners under Quasi-Static Loading

By

ERSHAD FORGHANY

THESIS

Submitted in partial satisfaction of the requirements for the degree of

MASTER OF SCIENCE

in

Mechanical and Aerospace Engineering

in the

OFFICE OF GRADUATE STUDIES

of the

UNIVERSITY OF CALIFORNIA

DAVIS

Approved:

Valeria La Saponara, Chair

Mohamed M. Hafez

Iman Soltani

Committee in Charge

2024

ACKNOWLEDGEMENTS

I dedicated this thesis to my Baba (Mahmoud), Grandpa Abbas, and Grandma Parirokh. My Maman (Marzieh), Grandpa Khalil, and Grandma Fatemah. My brothers Ehsun and Easar have been my role models. My special thanks to my advisor and thesis committee chair, Dr. Valeria La Saponara, committee members, Dr. Mohamed M. Hafez and Dr. Iman Soltani, my mentor at Sandia National Laboratories, Dr. Andrew Stershic, as well as the Department of Mechanical and Aerospace Engineering.

TABLE OF CONTENTS

Page

LIST OF TABLES

LIST OF FIGURES

LIST OF ACRONYMS/ABBREVIATIONS

GLARE Glass Laminate Aluminum Reinforced Epoxy

FML fiber metal laminate

LPF load proportionality factor

FEA Finite Element Analysis

FEM Finite Element Method

CLT Classical Laminated Theory

LTB Lateral-Torsional Buckling

V&V Verification and Validation

ASTM American Society for Testing and Materials

LVIs low-velocity impacts

FML Fiber Metal Laminate

S4R four-node shell element with reduced integration

S8R eight-node shell element with reduced integration

UTM Universal Testing Machine

RP reference points

IGS Initial Graphics Exchange Specification

CSV comma-separated value

PLA Polylactic Acid

PHA Polyhydroxyalkanoate

MMCs Metal Matrix Composites

ABSTRACT

This thesis investigates the enhancement of crashworthiness and structural integrity in Glass Laminate Aluminum Reinforced Epoxy (GLARE) channel section beams through the introduction of cross stiffeners. The ultimate goal is to improve crashworthiness, with a specific focus on the comparatively longer and gradual process of buckling and post-buckling analysis under compressive loads, rather than conducting a classical impact analysis. The study's methodology integrates a literature review with advanced numerical modeling using ABAQUS, validated by experimental benchmarking. The ABAQUS eigenbuckling and Riks analyses are meticulously validated against experimental data, achieving minimal error margins for buckling loads (3.5% - 5.2%), which are well below the allowable 10% error margin, and accurately matching failure modes. The introduction of cross stiffeners in the GLARE channel beam effectively recreates the mode shape concentrated at the mid-span of the beam, decreasing the buckling load by 39% compared to the no-stiffener configuration, potentially creating a crumple zone and maximizing energy absorption during high impact tests. Additionally, a more distributed failure pattern, controlled deformation, and a higher and longer post-buckling path are achieved, indicating improved stability and load-bearing capacity, with a 36% increase in failure load compared to the no-stiffener configuration. These findings demonstrate significant improvements in damage tolerance and provide a solid motivation for future work to test the crashworthiness of GLARE structures with cross stiffeners in aerospace applications, such as airframes and subcomponents, to better protect occupants.

Chapter 1. Foundations: Introduction, Comprehensive Literature Review, and Initial Research

1.1 Rationale for Progressing Glass Laminate Aluminum Reinforced Epoxy in Aerospace

Glass Laminate Aluminum Reinforced Epoxy (GLARE) is a thin-walled Fiber Metal Laminate (FML) material composed of alternating layers of aluminum and glass fiber-reinforced epoxy [1]. It has gained significant attention in the aerospace industry due to its unique combination of properties that are highly advantageous for modern aircraft design [2]: GLARE exhibits exceptional fatigue and impact resistance compared to traditional monolithic aluminum alloys such as the 2024-T3 alloy [3]. The hybrid nature of GLARE, which combines layers of aluminum with fiber-reinforced epoxy, allows it to withstand cyclic loading more effectively [4, 5].

GLARE has been shown to have superior performance in terms of crack growth resistance under fatigue loading [6]. In multi-axial fatigue loading scenarios, such as enduring shear alongside recurrent tensile stresses, GLARE demonstrates improved resistance to crack propagation [7]. Analytical, numerical, and experimental studies have highlighted GLARE's ability to slow down crack growth through its layered structure [8, 9]. The fiber-bridging effect in GLARE helps to arrest crack growth, reduce the rate of crack propagation [10], and distribute impact energy over a larger area [11], reducing the severity of damage from impacts such as bird strikes or ground handling incidents [12].

Moreover, the adoption of GLARE in aerospace is driven by its high strength-to-weight ratio [13], which is crucial for weight reduction—a key objective in aircraft design that directly impacts fuel efficiency and operational costs [14]. GLARE's excellent damage tolerance and impact resistance, combined with its high strength-to-weight ratio, enhance the crashworthiness of aircraft, which refers to the ability of aircraft structures and onboard systems to protect its occupants during an impact [15]. The layered structure of GLARE helps to absorb and dissipate energy during an impact, reducing the severity of damage and improving the survivability of the structure [16]. This is particularly important in critical areas such as fuselage skins, where maintaining structural integrity during a crash can prevent catastrophic failure and protect passengers [17, 18].

GLARE has been successfully implemented in various aircraft, demonstrating its reliability and effectiveness in real-world applications. For example, GLARE material is employed in the primary fuselage skin, with 27 GLARE skin panels spanning a combined area of 469 square meters on the upper fuselage skin of the Airbus A380, resulting in a weight reduction of 794 kg. It is also used in the leading edges of the horizontal and vertical stabilizers [19, 20, 21]. Additionally, GLARE is selected for the Boeing 777 bulk cargo floors and engine cowlings to enhance impact resistance [20, 22, 23]. The positive performance and durability observed in these applications provide a strong rationale for the further adoption and development of GLARE in future aerospace research.

1.2 Literature Review

Despite significant progress in the aerospace structures field, the use of stiffeners to improve damage tolerance and buckling resistance in thin-walled composites remains underexplored in academia.

Yang et al. [24] demonstrated that longitudinal stiffeners significantly enhance the performance of I-shaped steel beams, showing an 82% increase in flexural capacity and a reduction in lateral displacement and failure twist angle during Lateral-Torsional Buckling (LTB). Prado et al. [25] explored glass fiber-reinforced epoxy stiffeners in I-beams, noting a 207% increase in flange local buckling strength with optimally spaced stiffeners. Guo et al. [26] observed a 20.88% increase in the first-ply-failure load in carbon fiber-reinforced epoxy C-beams with L-shaped stiffeners and hole cutouts under off-center loads.

The extensive body of literature on aerospace structural elements, such as beam sections, provides valuable insights into the mechanical performance of composite structures. These studies highlight the influence of various laminate configurations, damage impacts, material properties, and failure criteria on the structural behavior of thin-walled composites. This enriched understanding of composite materials underscores their potential for real-world applications and sets the stage for further investigation into performance enhancements.

Gliszczynski and Kubiak [27] significantly contributed to this field by assessing the load capac-

ity of glass fiber-reinforced epoxy laminate C-shaped composite columns under uniform compression. They investigated three-ply configurations representing diverse laminate behaviors including quasi-isotropic, quasi-orthotropic, and angle-ply orientations. Their experimental setups, adhering to American Society for Testing and Materials (ASTM) standards, involved uniform compression and displacement monitoring, with corresponding Ansys numerical models closely replicating these conditions. The strong correlation between experimental and numerical results validated the simulation models' effectiveness in capturing real-world behavior.

Building on the previous work, Gliszczynski et al. [28] explored the impact of low-velocity impacts (LVIs) on pre-damaged, thin-walled composite channel-section columns made of glass fiber-reinforced epoxy laminate. They used the same lay-up configurations and added two more quasi-isotropic configurations, resulting in a comprehensive analysis. Their findings revealed minor variations in buckling and failure loads due to LVIs, with angle-ply systems occasionally exhibiting increased loads. The research highlighted the resilience of composite structures post-damage and their reliability in practical applications.

Expanding on Gliszczynski et al.'s work, Debski et al. [29] delved into numerical models of the nonlinear stability of thin-walled composite struts subjected to LVIs. They focused on the quasi-isotropic [0/-45/45/90]s layup configuration, named C1, and assessed the impacts of various damage scenarios on stability and post-buckling behavior. Using ABAQUS, they evaluated different models to determine their effects on material rigidity and buckling load. Their comprehensive analysis of damage effects on the structural integrity of composite struts validated the results and enriched the understanding of pre-damage impacts on composite materials.

Debski and Jonak [30] studied the post-buckling elastic behavior of carbon/epoxy composite channel section columns. They used the Tsai-Wu failure prediction criterion in ABAQUS, which accurately captured the complex interactions between different stress components. Their numerical results closely aligned with experimental data, highlighting the necessity for comprehensive failure criteria in understanding composite material behavior, crucial in industries like aviation and automotive.

Banat and Mania [31] investigated the stability and failure of thin-walled GLARE Z-shape and channel cross-sections under axial loading. Their study involved experimental tests across five layup configurations and numerical simulations, focusing on various fiber alignments. The Finite Element Analysis (FEA) results closely matched experimental data, especially for Z-sections. Their research highlighted the importance of aluminum layers and fiber alignment on critical loads, providing valuable insights for FEA structure design.

Banat et al. [32] further investigated the load-carrying capacity and stress state failure of thin-walled GLARE composite members under axial loading in the post-buckling range. They used experimental tests across two layup configurations and FEA simulations to assess top-hat GLARE sections. The study highlighted critical stresses leading to aluminum plastic deformation and intra-laminar failure in composite plies, emphasizing the robustness of the simulation models.

Mania and York [33] examined buckling strength improvements for GLARE in thin-walled open cross-section profiles across ten layup configurations using thin-ply material technology. Their research showed that thin-ply designs achieved significant increases in post-buckling strength compared to traditional FML configurations, highlighting the benefits of thin-ply technology for enhancing FML mechanical properties in aerospace applications.

Zaczynska and Mania [34] investigated dynamic buckling in thin-walled GLARE columns under axial compressive loading. Their study assessed the structure's resistance to dynamic pulse loading, considering initial geometric imperfections, stacking sequence, and pulse load shape. One specimen exhibited the greatest resistance to failure out of the three. The research highlighted the importance of dynamic buckling and failure criteria for GLARE structures, noting aluminum layer yielding as a primary failure mechanism.

Subbaramaiah et al. [16] evaluated the axial crushing response of GLARE top-hat structures across two layup configurations using experimental and numerical techniques. They measured crush force and energy absorption capabilities, finding that GLARE structures demonstrated superior performance compared to equivalent aluminum structures, highlighting their viability for crashworthy applications.

In summary, existing literature predominantly investigates various layup configurations and ply designs for channel and Z-section beams under axial loading, focusing on pre-buckling, post-buckling, and dynamic conditions, as well as damage tolerance. GLARE composites have shown exceptional resistance to failure, balancing the properties of aluminum and glass fiber-reinforced epoxy for crashworthy applications. However, a different approach is needed in research. Building on this foundation, this research aims to incorporate stiffeners into aerospace composite structural elements, such as channel section beams or C-beams, to evaluate enhancements in crashworthiness and structural performance during pre- and post-buckling. Specifically, this study aims to develop and validate numerical models using FEA software, ABAQUS, to assess the impact of stiffeners on the damage tolerance of GLARE C-beams. Additionally, it will investigate the effects of stiffener configurations on the structural behavior of composite thin-walled structures under pre- and post-buckling conditions as a proof-of-concept to demonstrate enhanced damage tolerance and increased crashworthiness of GLARE materials. It is important to note that this study does not involve classical impact tests; rather, it focuses on quasi-statically loading the beam over a relatively short period. While improved crashworthiness is the ultimate goal, this study lays the groundwork for future research to explore the full potential of GLARE materials in impact scenarios.

1.3 Introduction to Predicting Instabilities in Thin-Walled Composite Structures

Given the critical role of materials like GLARE in modern aerospace applications, it is essential to understand their behavior under various loading conditions, particularly under compressive stresses. While this thesis explores the numerical modeling and analysis of pre- and post-buckling behavior of GLARE C-beams, the mathematical overview will cover pre-buckling up to buckling, focusing on elasticity right before the onset of yielding to understand the choices made to assign the material properties in ABAQUS.

Buckling is a critical failure mode for slender structural elements under compressive stresses. It manifests as a sudden lateral deflection that can lead to catastrophic failure [35]. This behavior represents both a geometrical instability and a material failure. For example, in a slender beam

under unidirectional loading, buckling occurs when compressive stress reaches a critical level, causing the structure to deflect into a new configuration [35, 36].

To simplify the concept, consider the web section of a thin-walled C-beam under compression as shown in Figure 1.

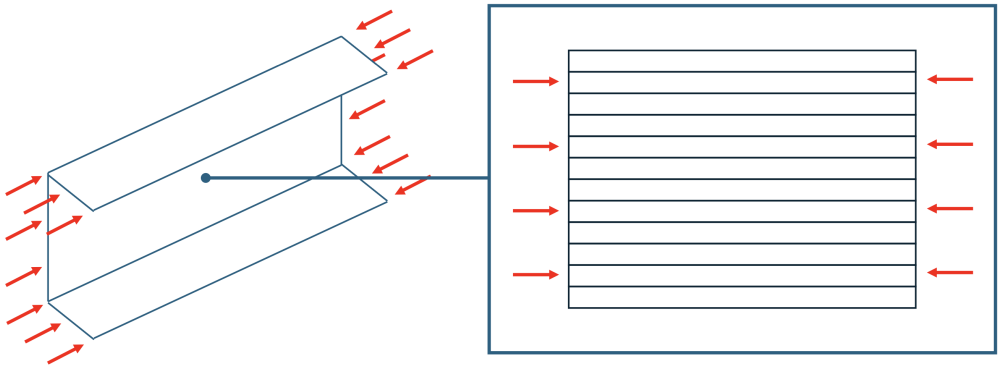

Figure 1: Web section of a thin-walled C-beam under axial compression.

This section now represents a thin plate. The anisotropic nature of GLARE, due to the glass fiber-reinforced epoxy laminates [37, 38], adds complexity to predicting buckling behavior because, instead of being isotropic, it is a special case of anisotropic material [39, 40]. More details on the nature of GLARE will be discussed in the subsequent chapter.

Buckling analysis in composite structures frequently employs Classical Laminated Theory (CLT), treating the laminate plate as a specific type of anisotropic laminae with directional properties tailored to complex load conditions, such as coupling effects that may occur in composite laminates [41]. From the web section taken from the C-beam in Figure 1, the modeling of a simply supported, special anisotropic plate under uniaxial compressive in-plane loading using CLT can be represented in Figure 2.

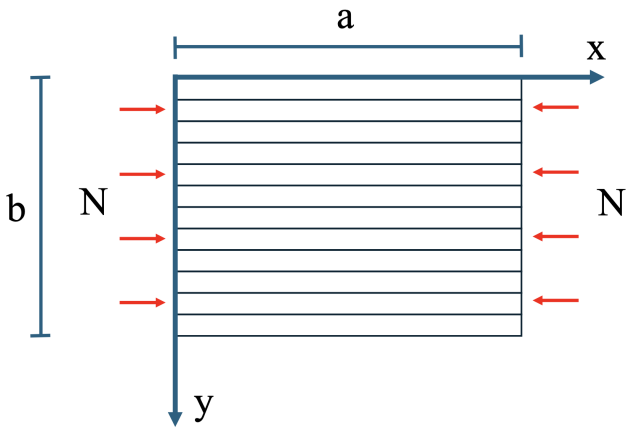

Figure 2: Special anisotropic plate experiencing directional compressive in-plane stress.

The critical buckling load, as shown in Figure 2, is given by the equation [41]:

$$N_{cr} = \frac{\pi^2}{a^2 m^2}\left[(D_{11}m^4 + 2(D_{12} + 2D_{66})(mnR)^2 + D_{22}(nR)^4)\right] \quad \mathrm{N} \tag{1}$$

where N_{cr} is the critical buckling load in newtons (N), a and b are the plate dimensions in millimeters (mm), D_{ij} are the bending stiffnesses in $\mathrm{N\,mm}$, and $R = a/b$ is unit-less. The buckling mode's configuration is defined by the indices m and n, which represent the number of half-sine waves along the x-coordinate and y-coordinate, respectively. As an example, for the loading case depicted in Figure 2, the bending stiffnesses can be expressed as [41]:

$$D_{11} = \frac{t^3}{12}\left(\frac{E_1}{1-\nu_{12}\nu_{21}}\right)\mathrm{N\,mm}, \quad D_{12} = \frac{t^3}{12}\left(-\frac{\nu_{12}E_2}{1-\nu_{12}\nu_{21}}\right)\mathrm{N\,mm}, \tag{2}$$

$$D_{22} = \frac{t^3}{12}\left(\frac{E_2}{1-\nu_{12}\nu_{21}}\right)\mathrm{N\,mm}, \quad D_{66} = \frac{G_{12}t^3}{12}\,\mathrm{N\,mm}. \tag{3}$$

Here, $E_1, E_2, G_{12}, \nu_{12}$, and ν_{21} represent the material's elastic and shear moduli in MPa, and Poisson's ratios in the local system (where 1 and 2 correspond to x and y, respectively, in Figure 2). The relationship between the Poisson's ratios is given by [41]:

$$\nu_{21} = \frac{E_2}{E_1}\nu_{12}$$

These stiffness coefficients D_{ij} are significantly affected by the anisotropy of the composite,

demonstrating how material properties and structural design influence the buckling behavior under specific loading scenarios [41]. The minimum buckling load corresponds to $n = 1$, and determining the minimum load for any given m requires knowledge of the D_{ij} coefficients and the plate dimensions a and b.

The prediction of buckling loads in composites is extensively studied both theoretically and experimentally. Research efforts, like those by Hatcher and Tuttle, strive to validate theoretical models against experimental data, highlighting the challenges in predicting composite panel buckling responses [41]. Although theoretical models offer a fundamental understanding, they may diverge from experimental findings due to idealized assumptions, complex real-world boundary conditions, and material property variabilities [41, 42].

Detailed analyses often utilize numerical methods, such as the Rayleigh-Ritz or Galerkin Finite Element Method (FEM), using commercial codes like ABAQUS [43]. These methods are particularly useful when closed-form solutions, like Equation 1, are impractical due to material anisotropy and structural geometry complexities [41, 44]. Instead, the governing equation of the plate buckling problem with coupling out-of-plane effects needs to be used [41]:

$$\begin{aligned} D_{11}\frac{\partial^4 w}{\partial x^4} + 4D_{16}\frac{\partial^4 w}{\partial x^3 \partial y} + 2(D_{12}+2D_{66})\frac{\partial^4 w}{\partial x^2 \partial y^2} + 4D_{26}\frac{\partial^4 w}{\partial x \partial y^3} + D_{22}\frac{\partial^4 w}{\partial y^4} \\ - B_{11}\frac{\partial^3 u^0}{\partial x^3} - 3B_{16}\frac{\partial^3 u^0}{\partial x^2 \partial y} - (B_{12}+2B_{66})\frac{\partial^3 u^0}{\partial x \partial y^2} - B_{26}\frac{\partial^3 u^0}{\partial y^3} \\ - B_{16}\frac{\partial^3 v^0}{\partial x^3} - (B_{12}+2B_{66})\frac{\partial^3 v^0}{\partial x^2 \partial y} - 3B_{26}\frac{\partial^3 v^0}{\partial x \partial y^2} - B_{22}\frac{\partial^3 v^0}{\partial y^3} \\ = q(x,y) + N_x\frac{\partial^2 w}{\partial x^2} + 2N_{xy}\frac{\partial^2 w}{\partial x \partial y} + N_y\frac{\partial^2 w}{\partial y^2} \end{aligned} \tag{4}$$

where the coupling of the in-plane forces are N_x, N_y, N_{xy}, the coupling stiffness matrix is B, the out-of-plane displacements are w, and the distributed load is $q(x, y)$. Eigenbuckling analysis can numerically solve buckling problems but assumes linear elastic behavior of materials up to buckling. This means it maintains a linear stress-strain relationship and excludes any plastic deformations before buckling occurs [45, 46]. Therefore, post-buckling analysis, such as the Riks method, is essential as it provides insights into structural behavior beyond the initial buckling event [47].

This stage involves large displacements, material and geometric nonlinearities, and imperfections, which the Riks method accommodates [48, 49].

In this thesis, the Riks method is utilized to investigate the post-buckling response, allowing for a detailed understanding of the stability and resilience of GLARE C-beams under compressive loads [50]. This comprehensive approach, integrating both buckling and post-buckling analyses, ensures a thorough assessment of GLARE materials' performance in crashworthy aerospace structures [51, 52].

Chapter 2. Numerical Linear and Nonlinear Buckling Analysis and Benchmarking

A comprehensive examination of the numerical modeling process, underpinned by rigorous benchmarking strategies, is presented to ensure the accuracy and reliability of the computational analysis of GLARE C-beams. The section meticulously details the development and refinement of a numerical model, emphasizing the critical alignment with experimental benchmarks to validate the simulation outcomes. Through a systematic approach that includes geometry definition, material property characterization, and boundary condition application, this section unfolds the layers of complexity involved in simulating the real-world behavior of composite structures. This endeavor not only serves as a cornerstone for the subsequent analytical phases but also establishes a robust framework for investigating the effects of perforations and geometric enhancements on the structural integrity of GLARE C-beams.

2.1 Numerical Modeling

The numerical model of the GLARE C-section beam under compressive loading, created using ABAQUS, was developed to establish a benchmarking foundation. This approach facilitates a clear assessment of the beam's inherent structural behavior, serving as a critical reference point against which the effects of subsequent modifications can be measured. This baseline model is essential for validating the computational analyses and ensuring that the simulations reliably reflect the beam's performance as reported by Banat and Mania [31].

2.1.1 Beam Geometry and Dimensions

The GLARE C-section beam was modeled with precise dimensions: 300 mm in length, 40 mm in width, and 80 mm in height, and the radius (R) at the junction of the web and the flange is approximately 1.75 mm. The total thickness of the composite is 1.9 mm. Details of the GLARE layers, which are further discussed in the following section, align with the physical specimens used by Banat and Mania [31] and are used for Verification and Validation (V&V). Figure 3 shows the

dimensions of the GLARE C-section beam as configured for the compression test.

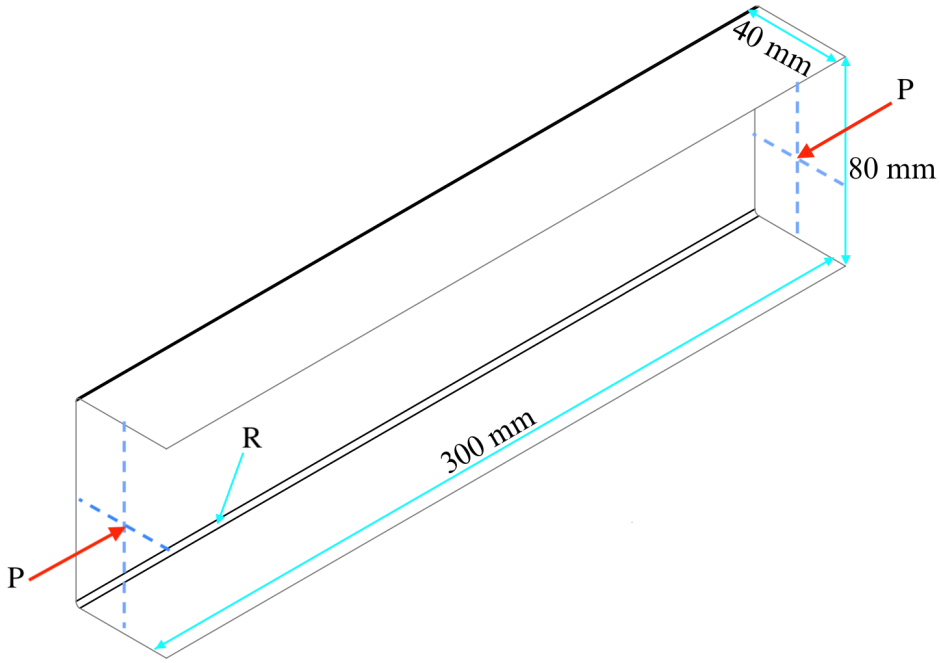

Figure 3: Composite beam schematic, with a fillet radius (R) of 1.75 mm and a load of (P).

The beam model was initially created in SOLIDWORKS and subsequently saved as an Initial Graphics Exchange Specification (IGS) file, a format chosen for its broad compatibility across different software platforms. This IGS file was then imported into ABAQUS for further analysis and simulation purposes.

2.1.2 Composite Behavior and Modeling

The GLARE laminate is composed of seven layers, featuring alternating plies of aluminum and fiber-reinforced composite. The aluminum used is a Al2024-T3 alloy, with each layer being 0.3 mm thick. The composite plies consist of glass-epoxy unidirectional fiber-reinforced prepreg TVR 380 M12 26% R-glass (Hexcel™), also referred to simply as R-Glass/Epoxy [31]. For all fiber-metal laminate (FML) configurations, a 3/2 stacking sequence is employed, where '3' represents three aluminum layers and '2' denotes two composite layers sandwiched between the aluminum sheets. The web and flanges consist of seven GLARE plies, each with a distinct fiber orientation, as depicted in as shown in Figure 4.

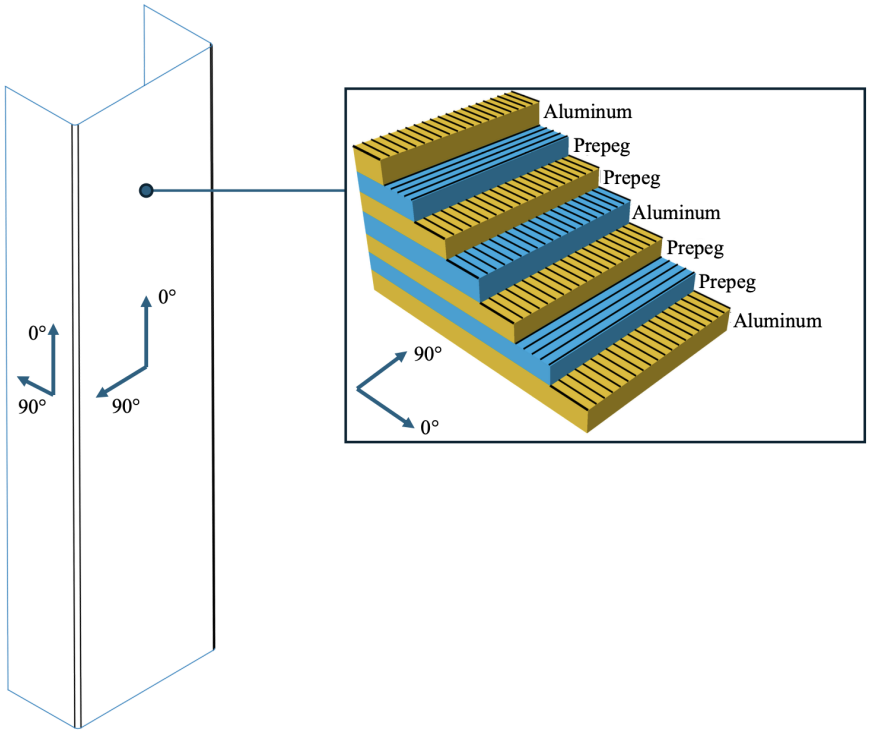

Figure 4: C2 laminate layering configuration of C-beam

This layup is modeled based on the orientations proposed by Banat and Mania for the C1-C5 beams, where all ply configurations are designed to align their orthotropic principal axes either parallel ($0°$—longitudinal fibers) or at a $45°$ angle ($90°$—transverse fibers) to the C-beam's wall edges. Aluminum is isotropic, but when defining the composite properties of the C-beam in ABAQUS, an arbitrary fiber direction must be assigned, which is set to $0°$. Banat and Mania conducted tests on five laminate configurations, as detailed in Table 1.

Table 1: Examined Configurations of Layer Sequences and Their Concise Notation [31]

C-section Beam Layups
C1 [AL/0/90/AL/90/0/AL]
C2 [AL/90/0/AL/0/90/AL]
C3 [AL/45/0/AL/0/45/AL]
C4 [AL/0/45/AL/45/0/AL]
C5 [AL/0/0/AL/0/0/AL]

For the general numerical modeling approaches and development, configuration C2 will be primarily used. This selection establishes a foundation for a detailed exploration of the mechani-

cal and physical characteristics of these laminates. Subsequently, V&V will be conducted across all configurations, but only the buckling load values will be considered, as Banat and Mania provided mode shapes only for the C2 configuration. This is why C2 was selected over the other configurations in Table 1.

2.1.2.1 Mathematical Modeling Overview of Composite Laminate Behavior

Inside the GLARE laminates the R-Glass/Epoxy plies, are transversely isotropic materials, exhibiting unique orthotropic properties [53]. A single R-Glass/Epoxy unidirectional ply, defined within its $(1, 2, 3)$ principal coordinate system, demonstrates symmetry in the $(2, 3)$ plane, as depicted in Figure 5.

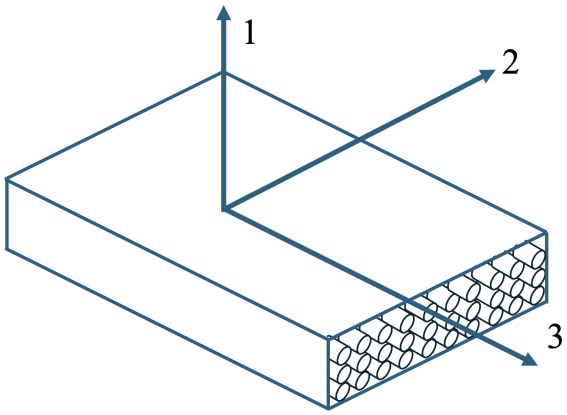

Figure 5: Orthotropic lamina with glass fibers in an epoxy matrix, 2-3 plane symmetry.

This schematic highlights the transversely isotropic nature of the polymer, reinforced by parallel glass fibers aligned with the 1-axis. The strength and stiffness peak in the direction parallel to the fibers (1-direction), while the $(2, 3)$ plane exhibits a uniform response due to the material's symmetry. In this plane, the material behaves isotropically, equating the properties in the 2-direction with those in the thickness direction (3-axis), which simplifies the structural analysis by reducing the number of independent constants in the stiffness matrix [54].

The generalized 3D linear elastic Hooke's law for the stress-strain relationship is formulated as [41]:

$$\begin{Bmatrix} \sigma_1 \\ \sigma_2 \\ \sigma_3 \\ \tau_{23} \\ \tau_{31} \\ \tau_{12} \end{Bmatrix} = \begin{bmatrix} C_{11} & C_{12} & C_{13} & 0 & 0 & 0 \\ & C_{22} & C_{23} & 0 & 0 & 0 \\ & & C_{33} & 0 & 0 & 0 \\ & & & C_{44} & 0 & 0 \\ & SYM & & & C_{55} & 0 \\ & & & & & C_{66} \end{bmatrix} \begin{Bmatrix} \epsilon_1 \\ \epsilon_2 \\ \epsilon_3 \\ \gamma_{23} \\ \gamma_{31} \\ \gamma_{12} \end{Bmatrix} \text{ MPa} \tag{5}$$

Here, σ and τ denote the normal stress and shear stress components in MPa, respectively, while ϵ and γ represent the normal and shear strain components. The stiffness matrix C_{ij} in MPa relates these stress and strain components, with subscripts ij indicating the material's principal directions. The material's symmetry within the transverse 1-2 plane simplifies this relationship, allowing a reduction in the matrix's complexity.

Considering the theoretical predictions of buckling loads for an orthotropic ply, as discussed in Equation 1 from Section 1.3, a plane stress condition is assumed. This leads to a simplification of Equation 5 to a two-dimensional state, defining engineering constants as:

$$\begin{bmatrix} \sigma_1 \\ \sigma_2 \\ \tau_{12} \end{bmatrix} = \begin{bmatrix} Q_{11} & Q_{12} & 0 \\ Q_{21} & Q_{22} & 0 \\ 0 & 0 & 2Q_{66} \end{bmatrix} \begin{bmatrix} \epsilon_1 \\ \epsilon_2 \\ \gamma_{12}/2 \end{bmatrix} \text{ MPa} \tag{6}$$

where Q_{ij} are the stiffness coefficients in MPa within the lamina stiffness matrix that encapsulates the material properties. The relationships between the engineering constants and the stiffness coefficients are given by [41]:

$$Q_{11} = \frac{E_1}{1 - \nu_{12}\nu_{21}} \text{ MPa}, \quad Q_{12} = Q_{21} = \frac{\nu_{12}E_2}{1 - \nu_{12}\nu_{21}} \text{ MPa}, \tag{7}$$

$$Q_{22} = \frac{E_2}{1 - \nu_{12}\nu_{21}} \text{ MPa}, \quad Q_{66} = G_{12} \text{ MPa} \tag{8}$$

where E_1 and E_2 are the longitudinal and transverse elastic moduli in MPa, respectively; ν_{12} and ν_{21} are the major and minor Poisson's ratios, respectively; and G_{12} is the shear modulus in MPa. Q_{ij} is ubiquitously used throughout CLT to defined the mechanical behavior of lamina under loading as evident in Equation 1 where the bending stiffnesses expressed in 2 and 3 can re-expressed to:

$$D_{11} = \frac{Q_{11}t^3}{12}\,\mathrm{N\,mm}, \quad D_{12} = \frac{Q_{12}t^3}{12}\,\mathrm{N\,mm}, \quad D_{22} = \frac{Q_{22}t^3}{12}\,\mathrm{N\,mm},$$
$$D_{66} = \frac{Q_{66}t^3}{12}\,\mathrm{N\,mm}$$

A comprehensive explanation of the derivations of Equations 5 to 8 and their implications is available in Appendices A.1 through A.3.

Each laminate possesses a principal, or global, coordinate system (x, y, z) and has plies in their own non-principal, or local, coordinate systems $(1, 2, 3)$ due to the orientation of each lamina, θ, as illustrated in Figure 6.

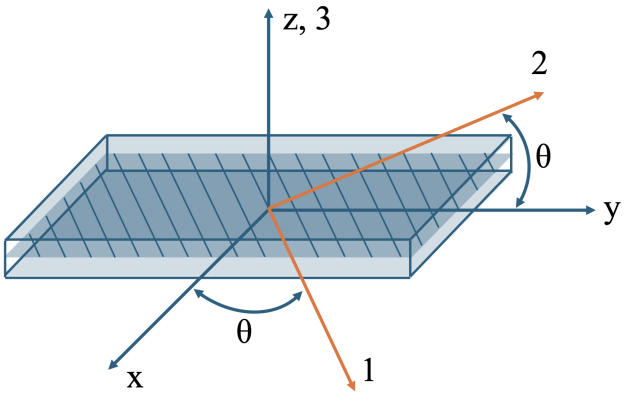

Figure 6: Laminate global (x, y, z) coordinates vs. ply local $(1, 2, 3)$ coordinates.

Therefore, the concept of plane stress transformation becomes crucial here. The resulting stress and strain components of each lamina, as defined in Equation 6, must be transformed into the global components to account for the fiber orientation. This transformation is accomplished using the following relation [41]:

$$\begin{Bmatrix} \sigma_x \\ \sigma_y \\ \tau_{xy} \end{Bmatrix} = \begin{bmatrix} \overline{Q}_{11} & \overline{Q}_{12} & \overline{Q}_{16} \\ \overline{Q}_{12} & \overline{Q}_{22} & \overline{Q}_{26} \\ \overline{Q}_{16} & \overline{Q}_{26} & \overline{Q}_{66} \end{bmatrix} \begin{Bmatrix} \epsilon_x \\ \epsilon_y \\ \gamma_{xy} \end{Bmatrix} \quad \text{MPa} \tag{9}$$

where $c = \cos\theta$ and $s = \sin\theta$, and θ is in degrees ($^\circ$). The components $\overline{Q}_{ij}$ refer to the elements of the transformed lamina stiffness matrix in MPa, which are defined [41]:

$$\begin{aligned}
\overline{Q}_{11} &= Q_{11}c^4 + Q_{22}s^4 + 2(Q_{12} + 2Q_{66})s^2c^2 \quad \text{MPa} \\
\overline{Q}_{12} &= (Q_{11} + Q_{22} - 4Q_{66})s^2c^2 + Q_{12}(c^4 + s^4) \quad \text{MPa} \\
\overline{Q}_{22} &= Q_{11}s^4 + Q_{22}c^4 + 2(Q_{12} + 2Q_{66})s^2c^2 \quad \text{MPa} \\
\overline{Q}_{16} &= (Q_{11} - Q_{12} - 2Q_{66})c^3s - (Q_{22} - Q_{12} - 2Q_{66})cs^3 \quad \text{MPa} \\
\overline{Q}_{26} &= (Q_{11} - Q_{12} - 2Q_{66})cs^3 - (Q_{22} - Q_{12} - 2Q_{66})c^3s \quad \text{MPa} \\
\overline{Q}_{66} &= (Q_{11} + Q_{22} - 2Q_{12} - 2Q_{66})s^2c^2 + Q_{66}(s^4 + c^4) \quad \text{MPa}
\end{aligned}$$

Alternatively, the strains can be expressed in relation to the stresses as follows:

$$\begin{Bmatrix} \epsilon_x \\ \epsilon_y \\ \gamma_{xy} \end{Bmatrix} = \begin{bmatrix} \tilde{S}_{11} & \tilde{S}_{12} & \tilde{S}_{16} \\ \tilde{S}_{12} & \tilde{S}_{22} & \tilde{S}_{26} \\ \tilde{S}_{16} & \tilde{S}_{26} & \tilde{S}_{66} \end{bmatrix} \begin{Bmatrix} \sigma_x \\ \sigma_y \\ \tau_{xy} \end{Bmatrix} \tag{10}$$

The components $\tilde{S}_{ij}$ represent the elements of the transformed lamina compliance matrix in MPa^{-1}, which is defined by the inverse of the stiffness matrix $[Q]$. The transformed compliance matrix components are given by [41]:

$$\overline{S}_{11} = S_{11}c^4 + (2S_{12} + S_{66})s^2c^2 + S_{22}s^4 \quad \text{MPa}^{-1}$$

$$\overline{S}_{12} = S_{12}(s^4 + c^4) + (S_{11} + S_{22} - S_{66})s^2c^2 \quad \text{MPa}^{-1}$$

$$\overline{S}_{22} = S_{11}s^4 + (2S_{12} + S_{66})s^2c^2 + S_{22}c^4 \quad \text{MPa}^{-1}$$

$$\overline{S}_{16} = (2S_{11} - 2S_{12} - S_{66})s^3c - (2S_{22} - 2S_{12} - S_{66})s^3c \quad \text{MPa}^{-1}$$

$$\overline{S}_{26} = (2S_{11} - 2S_{12} - S_{66})s^3c - (2S_{22} - 2S_{12} - S_{66})s^3c \quad \text{MPa}^{-1}$$

$$\overline{S}_{66} = 2(2S_{11} + 2S_{22} - 4S_{12} - S_{66})s^2c^2 + S_{66}(s^4 + c^4) \quad \text{MPa}^{-1}$$

The detailed derivation of Equations 9 and 10 is available in Appendix A.3.3. The implementation of these theoretical principles in ABAQUS will now be examined.

2.1.2.2 Laminate Transformations in ABAQUS

Table 2 demonstrates the ABAQUS interface for defining the layup of each web and flange laminate in the beam (Figure 4).

Table 2: C2 Beam Web, Top, and Bottom Flanges Ply Properties and Orientation

Ply Name	**Region**	**Material**	**Thickness**	**CSYS**	**Rotation Angle**	**Integration Points**
Ply-1	(Picked)	Al2024-T3	0.3	⟨layup⟩	0	3
Ply-2	(Picked)	R-GlassEpoxy	0.25	⟨layup⟩	90	3
Ply-3	(Picked)	R-GlassEpoxy	0.25	⟨layup⟩	0	3
Ply-4	(Picked)	Al2024-T3	0.3	⟨layup⟩	0	3
Ply-5	(Picked)	R-GlassEpoxy	0.25	⟨layup⟩	0	3
Ply-6	(Picked)	R-GlassEpoxy	0.25	⟨layup⟩	90	3
Ply-7	(Picked)	Al2024-T3	0.3	⟨layup⟩	0	3

The 'Region' column represents the geometric part defined by the user for each respective web, top, and bottom flange, resulting in three laminates defined. Each ply corresponds to the selected geometric part for the laminate, which is why it is labeled as '(Picked)'. The 'CSYS' column corresponds to the discrete orientation that defines each laminate's global coordinate system in relation

to the global datum coordinate system, which serves as the reference point for the entire model and determines the orientation and location of all entities within the simulation. The 'Thickness' column specifies the ply thickness in mm. The 'Rotation Angle' column specifies the orientation of each lamina, θ in degrees ($^\circ$), to effectively transform the local stress and strain components of the ply to the global components of the laminate, guided by the theoretical framework of Equations 9 and 10, albeit ABAQUS employs a full 3D and higher-order analysis [55]. Figure 7 illustrates the layup for various structural elements of the C2 C-beam.

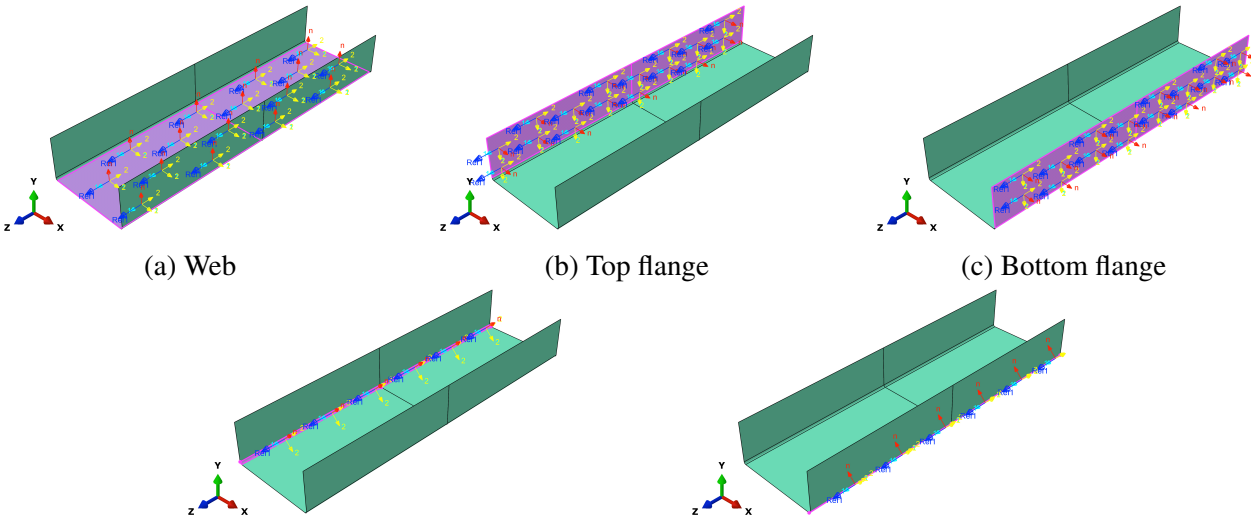

(a) Web (b) Top flange (c) Bottom flange

(d) Top fillet (e) Bottom fillet

Figure 7: Fiber orientations at 0° ply.

This includes the web (Figure 7a), the top flange (Figure 7b), the bottom flange (Figure 7c), bottom fillet (Figure 7e), and fop fillet (Figure 7d), each defined with its respective coordinate system. Figure 8 details the discrete orientation definitions in the global coordinate systems for each laminate. For the web laminate (Figure 8a), the normal vector is $(0.0, 1.0, 0.0)$, parallel to the y-axis, with the primary direction vector $(0.0, 0.0, 1.0)$ aligned with the z-axis. This sets the laminate global 3-axis as the global datum z-axis and the laminate global 2-axis as the global datum x-axis. Similarly, the top and bottom laminates (Figures 8b and 8c) feature normal vectors $(1.0, 0.0, 0.0)$ and primary direction vectors $(0.0, 0.0, 1.0)$, consistent with the datum global z-axis and x-axis, respectively. In contrast, for the top and bottom fillet laminates (Figures 8d and 8e), the normal vectors are de-

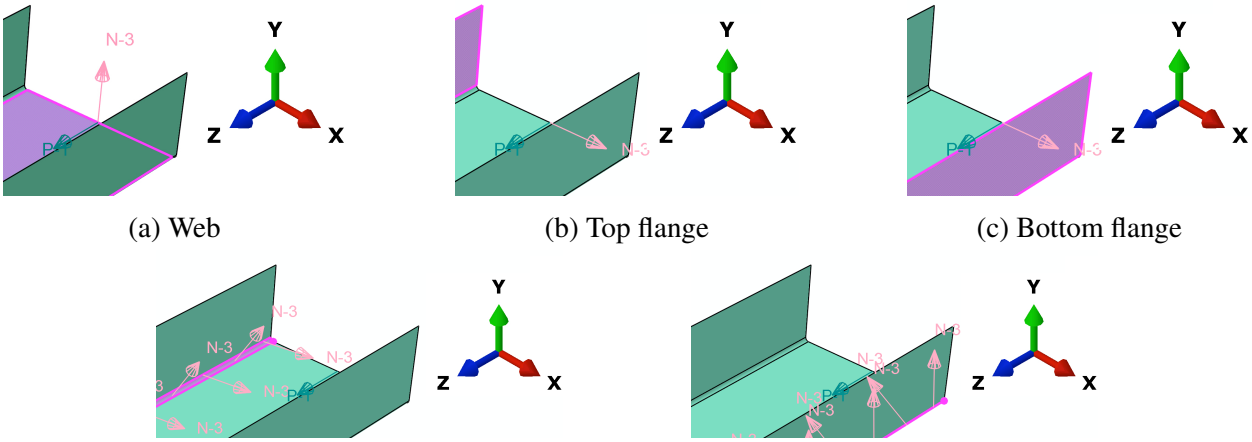

(a) Web (b) Top flange (c) Bottom flange

(d) Top fillet (e) Bottom fillet

Figure 8: Discrete orientations for local coordinate systems.

termined by the surfaces on the inside of the C-beam, with primary direction vectors $(0.0, 0.0, 1.0)$ consistently aligned with the datum global z-axis and x-axis, respectively.

The configuration of the C2 beam layup is shown in Figure 9, detailing the C-beam's web, flange, and fillet properties.

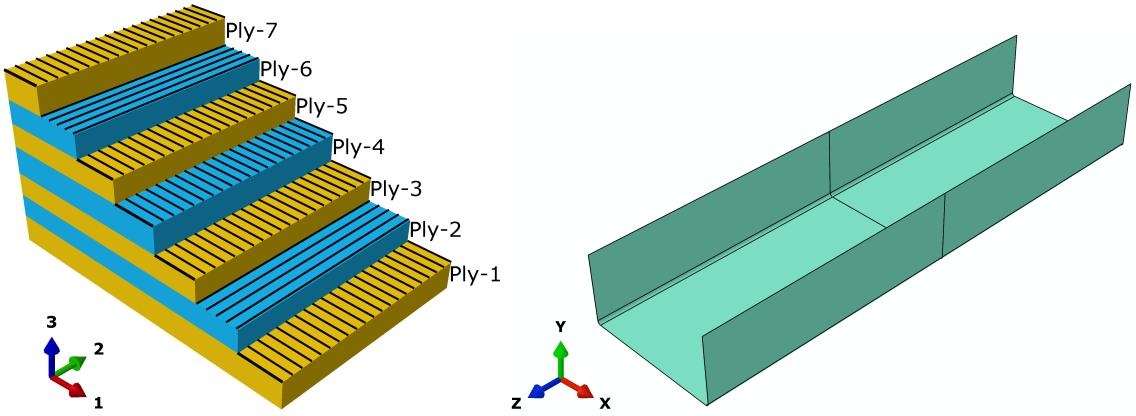

(a) Ply stack-up. (b) Isometric view.

Figure 9: C2 Layup configurations for C-beam: web, flange, and fillet properties in ABAQUS.

Figure 9a details each laminate in both the web and flange with respect to the properties and orientations defined in Table 2. The isometric view of the C-beam's complete laminated structure is showcased in Figure 9b, illustrating the consistent application of ply thicknesses, lamination stacks, and fiber orientations across all laminates.

The material properties of the Al2024-T3 alloy and the R-Glass/Epoxy prepreg were sourced from the research by Banat and Mania [31]. Kamocka et al. [56], co-authored with Mania, conducted bending tests on the prepreg using ASTM D 790-00 and tensile tests using ASTM D 3039/D 3039M-00. For Al2024-T3, the PN-EN ISO 6892-1 standards were applied [56]. Banat and Mania [31] incorporated these results into their numerical study parameters. Therefore, the elastic and plastic properties, including the strength properties of the R-Glass/Epoxy prepreg, are summarized in Tables 3-4, which are used for the numerical model laminates shown in Figure 9.

Table 3: Mechanical Properties of Al 2024-T3 and R-Glass/Epoxy [31, 56]

Property	Al 2024-T3	R-Glass/Epoxy
E_1 [MPa]	77000	53900
E_2 [MPa]	–	14920
G_{12} [MPa]	28950	5490
G_{23} [MPa]	–	5330
G_{13} [MPa]	–	5490
R_y [MPa]	359	–
ν_{12}	0.33	0.28
ν_{23}	–	0.40
ν_{13}	–	0.28

Table 4: Strengths of R-Glass/Epoxy [31]

Description	Strength [MPa]
X_t	1534
X_c	800
Y_t/Z_t	75
Y_c/Z_c	500
S	58

R_y is the yield strength where the stress is measured at a strain of 0.2% [56]. X_t is the longitudinal tensile strength, X_c is the longitudinal compressive strength, Y_t/Z_t is the transverse tensile strength, Y_c/Z_c is the transverse compressive strength, and S is the shear strength in the plane of the layer.

2.1.3 Boundary Condition Specifications

The comprehensive literature review in Chapter 1 highlighted recent advancements in numerical modeling techniques for C-beams under compression. Research efforts by Gliszczynski et al. [28], Debski and Jonak [30], and Banat and Mania [31] have focused on creating numerical models of experimentally tested C-beams in a Universal Testing Machine (UTM). Debski and Jonak [30] implemented constraints at both lower and upper sections of the beam, fixing translation such that movement perpendicular to each wall was restricted ($U_x = 0, U_y = 0, U_z = 0$). Banat and Mania [31], on the other hand, secured the constraints to the nodes, considering the flat bottom grooves in which the beam was seated. Debski and Jonak's [30] setup also featured a ball-and-socket joint allowing rotational freedom in the Y-direction, a characteristic that permits slight pivotal or rotational movement under load without sideways translation. Gliszczynski et al. [28] adopted a more sophisticated approach in modeling boundary conditions for C-beams, incorporating detailed considerations for various constraints and loading scenarios. Their simulation model not only demonstrates a clear visual representation of applied boundary conditions but also provides an insightful analysis of anticipated deformation under compressive load, as depicted in Figure 10.

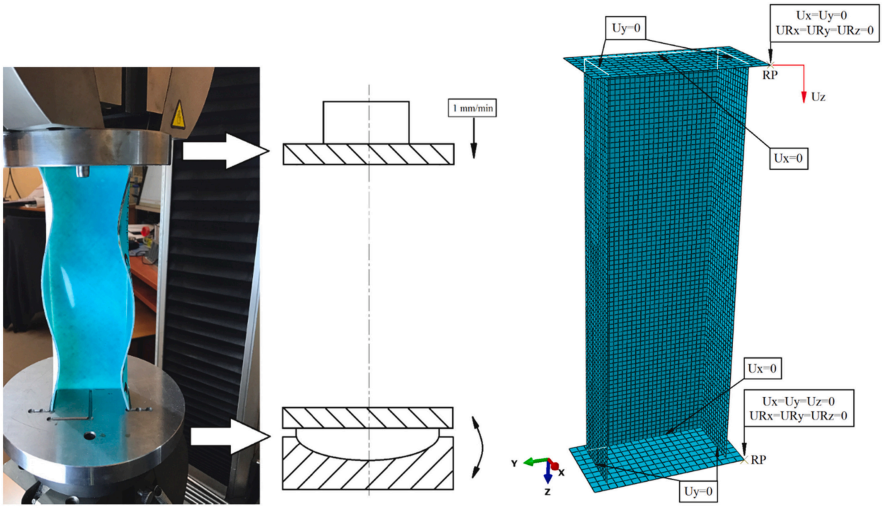

(a) Test stand. [28] (b) Boundary conditions. [28]

Figure 10: Gliszczynski et al.'s experimental mapping of boundary conditions to numerical model.

In this setup, the lower plate was fully constrained, restricting all degrees of freedom at the

reference points (RP), while the upper plate allowed movement solely in the Z-axis to simulate compressive loading. This design closely replicates an experimental UTM setup, where movement is limited to the direction of the applied load, thus ensuring a uniaxial compression state. The beam ends were simply supported, allowing rotational freedom while constraining movement perpendicular to the plane of the beam's web and flanges, as illustrated in Figure 10b. This approach maintains the structural integrity of the C-section during load application.

The accuracy of the simulation critically hinges on these boundary conditions, ensuring the numerical model mimics the physical constraints of the experimental setup. Gliszczynski et al. [28] further addressed contact interactions at the end-plate contacts, essential for accurately replicating stress distribution and deformation characteristics under load. The nodes at the C-beam edges were restrained from moving perpendicular to the its walls while allowing rotation, effectively capturing the behavior of the C-beam within the UTM. This detailed simulation approach enhances the reliability and validity of performance predictions, setting it apart from the methodologies used by Debski and Jonak [30] and Banat and Mania [31], where the compression plates were not modeled, possibly leading to discrepancies in results.

2.1.3.1 Coupling Constraints

In the current numerical model, a simplification is adopted, aiming to accurately reflect the effects of the compression plates used by Gliszczynski et al. [28], while streamlining the model. This simplification involves omitting the physical representation of the compression plates, instead using abstract coupling constraints [57, 58]. RP-1 and RP-2 are established at the center of the beam at both upper and lower ends (Figure 11).

These reference points serve as application sites for boundary conditions, effectively simulating the effects of the compression plates on the beam. Surface sets at the beam ends, highlighted in Figure 12 in red, correspond to areas of interaction with the compression plates.

Coupling constraints, necessary for accurately modeling interactions between structural components as depicted in Figure 13, link the surface displacements of the beam to specific reference

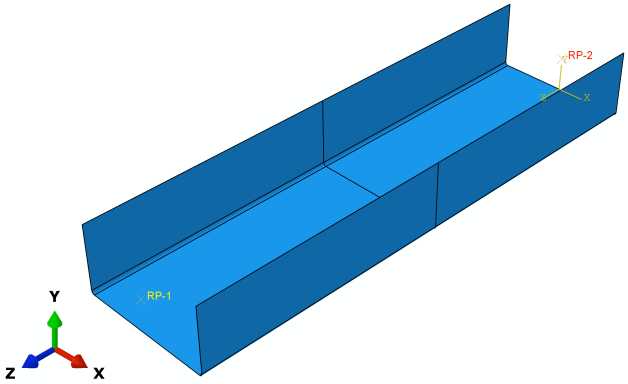

Figure 11: Assembly model indicating the reference points.

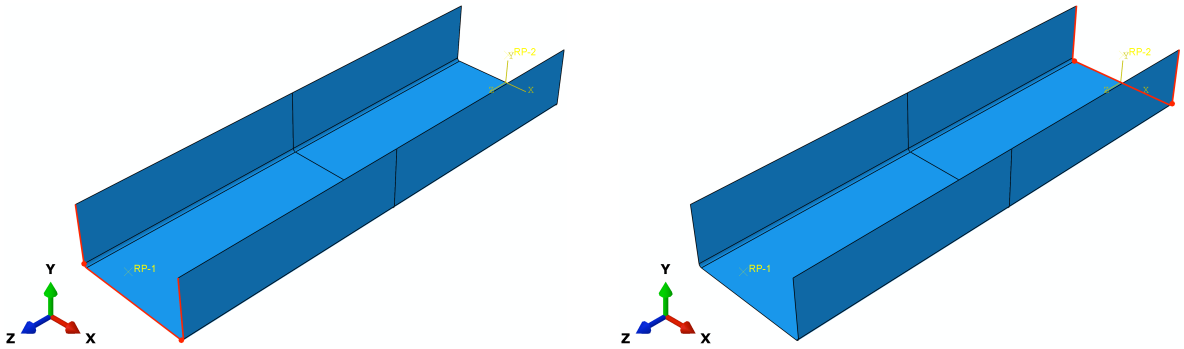

(a) Bottom surface set

(b) Top surface set

Figure 12: Illustration of surface sets

points.

The 'Control Points' (RP-1 and RP-2), marked in red, are where constraints are applied, regulating degrees of freedom in different model regions. The 'Surface', in magenta, consists of bottom and top surface sets (Figure 12) of the beam. This interaction establishes coupling constraints, governing the behavior of affected model areas in response to displacements at the control points during simulation [55].

The kinematic coupling constraints ensure uniform load distribution across the beam's width, facilitating precise control over displacement in specific degrees of freedom while preventing rotational movement [55]. This choice allows the displacements of the beam's top surface nodes to follow those of the reference point precisely, permitting displacement control in specific degrees of freedom, without rotational movement [55]. A key advantage of this modeling approach is its ability to factor in the influence of the plates without explicitly modeling them, thereby significantly

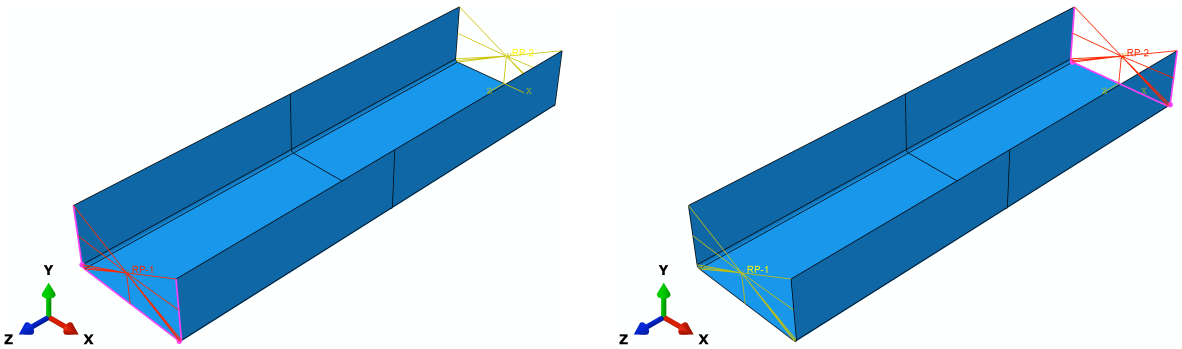

(a) Bottom constraint (b) Top constraint.

Figure 13: Kinematic coupling constraints

reducing the model's computational complexity.

2.1.3.2 Support Conditions

Figure 14 displays the support conditions of the beam, setting the stage for developing a robust numerical model with accurate boundary constraints.

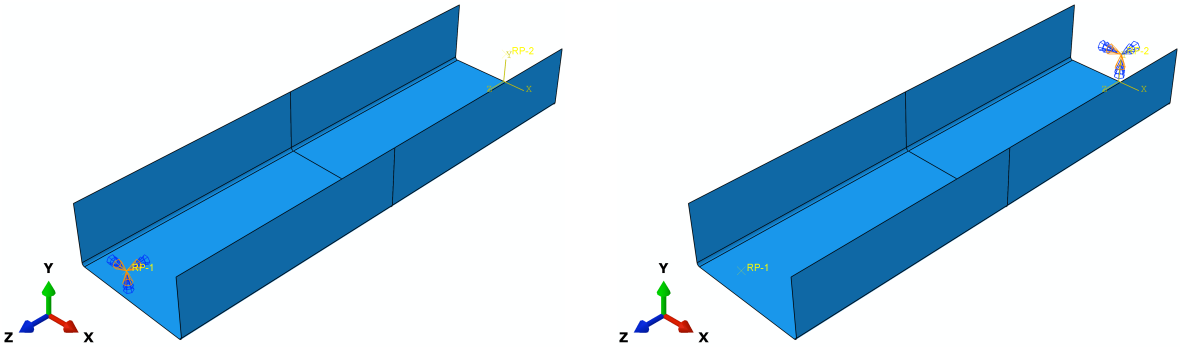

(a) Encastre at RP-1 (b) Displacement/Rotation at RP-2

Figure 14: Illustration of support boundary conditions.

In alignment with the methodology of Gliszczynski et al. [28], the beam's lower end is fully constrained at reference point RP-1. This mimics a fixed support condition, prohibiting all translations and rotations, akin to an encastre boundary condition (U1 = U2 = U3 = UR1 = UR2 = UR3 = 0). Figure 14a illustrates this setup, where small orange arrows indicate fixed translations and large blue arrows denote fixed rotations. Conversely, at the beam's upper end, RP-2 is constrained to simulate compressive loading (Figure 14b), limiting the upper plate's movement solely to the

z-axis (U3), similar to a displacement/rotation boundary condition (U1 = U2 = UR1 = UR2 = UR3 = 0). These constraints, defined in the 'initial step' of the analysis, establish the essential boundary conditions, predefined fields, and interactions at the start of the analysis [55]. They serve as the cornerstone for ensuring the accuracy and reliability of subsequent simulation results by correctly setting up the model's initial state and governing behavior.

2.1.3.3 Loading Conditions

A constant concentrated force of 1.0 N is applied in the z-axis (U3) direction at reference point RP-2, as depicted in Figure 15.

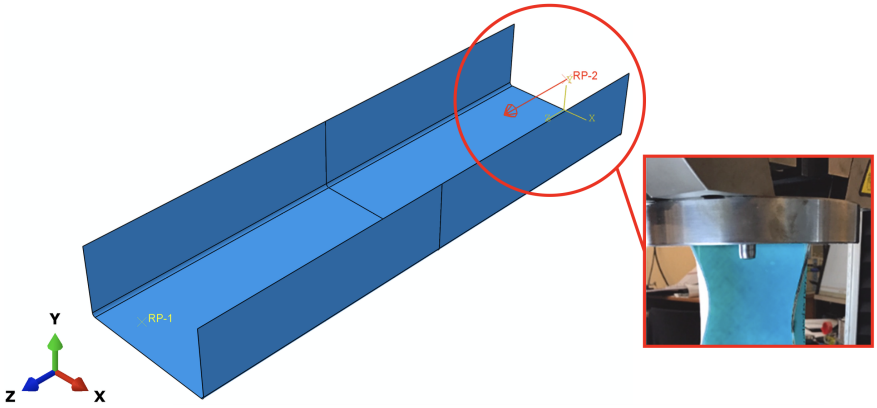

Figure 15: Application of concentrated force at RP-2 mimicking top plate compression [28].

This force simulates the compressive force exerted by the top plate on the beam [57] and is transferred to the beam's top surface via the kinematic coupling illustrated in Figure 13b, linking RP-2 to the corresponding beam surface nodes.

2.1.4 Eigenbuckling Analysis

Transitioning to the stability analysis setup, the numerical model incorporates eigenvalue buckling analysis in ABAQUS. This approach is grounded in solving an eigenvalue problem, which is foundational to linear perturbation theory. Subsequently, to capture the realistic behavior of the structure post-buckling, the Riks method is employed. This analysis phase is essential for understanding the large deflection responses of the structure and ensuring post-buckling stability.

2.1.4.1 General Eigenvalue Buckling

Eigenvalue buckling analysis determines the conditions that cause the stiffness matrix to become singular, resulting in nontrivial displacement solutions $\mathbf{v}^M$ with units of millimeters mm, as described by [55]:

$$K^{MN}\mathbf{v}^M = 0 \tag{11}$$

where K^{MN} represents the tangent stiffness matrix, in $\mathrm{N\,mm^{-1}}$, under unidirectional compressive forces, with M and N indicating the degrees of freedom. This method proves effective for stiff structures by identifying critical loads predominantly carried by axial loads or membrane actions, with minimal pre-buckling deformation [55, 59].

2.1.4.2 Base State and Eigenvalue Problem

Buckling loads are evaluated relative to the structure's base state, either the initial conditions or the state following the last general analysis step. The eigenvalue problem is articulated as [55]:

$$\left(K_0^{NM} + \lambda_i K_\Delta^{NM}\right)\mathbf{v}_i^M = 0 \tag{12}$$

with K_0^{NM} and K_Δ^{NM} denoting the stiffness matrices in the base state and those resulting from incremental loading Q^N in N, respectively, both with units of $\mathrm{N\,mm^{-1}}$. The stability threshold is indicated by the smallest significant eigenvalue λ_i, with eigenvectors $\mathbf{v}_i^M$ elucidating the ith potential failure modes, in mm.

2.1.4.3 Subspace Method

The subspace iteration method, tailored for extracting significant eigenmodes, refines the lowest eigenvalues and their corresponding eigenvectors through iterative processes [60]. Selected for its efficiency in pinpointing critical buckling modes, this method simplifies the analysis procedure [61]. The steps in ABAQUS for the eigenbuckling analysis include [55]:

1. Defining geometric and material properties.

2. Applying boundary conditions, considering the base state geometry aligns with the body's original configuration without initial preloads or geometric nonlinearity.

3. Initiating a linear perturbation analysis step for buckling.

4. Conducting the analysis using the subspace iteration method to ascertain critical load factors and buckling modes.

Focusing on the first buckling mode necessitates requesting a single eigenvalue. The setup specifies using two vectors per iteration, with a cap of 300 iterations, to thoroughly explore for the buckling load. Insights into the onset of instability and deformation patterns at buckling are derived from this analysis, leveraging Equations 11 and 12. Suitable for linear response scenarios, nonlinear methods like the Riks method are advised for analyses anticipating significant deformations under buckling loads.

The quasi-static loading conditions in the experimental study by Gliszczynski et al. on C-beams, performed in the UTM, underscore the subspace method's applicability to scenarios where static equilibrium assumptions are already valid [27, 62], offering valuable insights into instability onset and buckling deformation patterns.

2.1.5 Static Riks

After obtaining the critical buckling loads through eigenvalue buckling analysis, the load applied during the nonlinear analysis phase is scaled according to the smallest eigenvalue obtained. This scaling adjusts the initial 1.0 N load from Figure 15 to match the critical load, providing a realistic basis for assessing the structure's response under actual buckling conditions.

2.1.5.1 Arc Length Method and Control

The static Riks method, also defined as the arc-length method, captures softening behavior while using load control [63]. In a Riks step, the loading remains proportional throughout any increment.

The current load magnitude, P_{total}, is calculated as [55]:

$$P_{total} = P_0 + \lambda_f (P_{ref} - P_0) \tag{13}$$

where P_0 is the initial load, P_{ref} is the reference load vector, and λ_f is the load proportionality factor (LPF) dynamically computed as part of the solution. P_{ref} is defined as a prescribed load, explicitly defined and applied to the structure. All loads are ramped from their initial values, P_0, to the specified reference loads, P_{ref}, and beyond P_{ref} if not terminated manually or by user-defined criteria.

In ABAQUS, the Riks method employs Newton's method to solve the nonlinear equilibrium equations [55, 64, 65]:

$$\mathbf{R}(\mathbf{u}) = \mathbf{F}_{\text{ext}} - \mathbf{F}_{\text{int}}(\mathbf{u}) = 0 \tag{14}$$

$$\mathbf{F}_{\text{int}}(\mathbf{u}^{(\mathbf{k+1})}) = \mathbf{F}_{\text{int}}(\mathbf{u}^{(\mathbf{k})}) + \mathbf{J}^{-1}(\mathbf{u}^{(k)})\Delta\mathbf{u}^{(k)} = \mathbf{F}_{\text{ext}} \tag{15}$$

where $\mathbf{R}(\mathbf{u})$ is the residual vector, $\mathbf{F}_{\text{int}}(\mathbf{u})$ is the internal force vector, which is a function of the displacements $\mathbf{u}$, and $\mathbf{F}_{\text{ext}}$ is the external force vector. Moroever, $\mathbf{u}^{(k)}$ is the displacement vector at iteration k, $\mathbf{J}(\mathbf{u}^{(k)}) = \left(\frac{\partial \mathbf{F}_{\text{ext}}}{\partial \mathbf{u}}\right)^k$ and is the Jacobian matrix (or tangent stiffness matrix) at iteration k, and $\Delta\mathbf{u}^{(k)}$ is the displacement increment of the solution. This technique relies on a 1% extrapolation of the strain increment to control incrementation [66]. The initial arc length increment establishes the scale for subsequent steps, enabling precise control over the solution's progression along the equilibrium path [55]:

$$\Delta\lambda_{\text{in}} = \frac{\Delta\lambda_{\text{in}}}{l_{\text{period}}} \tag{16}$$

Here, $\Delta\lambda_{\text{in}}$ represents the initial increment in the arc length, and l_{period} is a user-specified total arc length scale factor, typically set equal to 1. The initial load proportionality factor, $\Delta\lambda_{\text{in}}$, is

computed based on this value. Configuring the Riks method in ABAQUS involves the following steps [55]:

1. Establishing initial and boundary conditions based on the unloaded geometry of the structure.

2. Defining material properties that accommodate nonlinearity and specifying options for geometric nonlinearity to manage large deformations.

3. Selecting the Riks analysis step and setting parameters such as the total arc length, initial step size, and controls for incrementation.

4. Monitoring the analysis for convergence issues, especially during transitions through unstable paths, and adjusting solver settings as necessary to ensure accurate tracing of the equilibrium path.

The setup configures the incrementation to be automatic, with a maximum number of iterations set to 1000. The default is set to 100, and the license constraint is 10000. This configuration ensures that the solution is accurate and stable without using excess computational resources [55]. The arc length increments start with an initial value of 0.01, with a minimum of 1×10^{-6} and a maximum of 1×10^{36}, and a total arc length of 1. In the unloaded geometry scenario, the primary buckling mode shape derived from eigenbuckling analysis is transferred to the geometric profile through the Riks method, setting an initial imperfection at 0.01 times the total wall thickness.

It should be noted that observing negative increments in the arc length is indicative of structural failure, particularly in scenarios involving buckling or post-buckling behavior [67, 68]. This condition is often associated with significant structural damage or failure. When this is observed, the simulation will be terminated as it indicates the failure mode [67].

From this analysis, the LPF versus arc length history plot can be derived, leveraging Equations 13 & 16. The LPF can then be used to multiply the critical buckling load to obtain a more accurate critical buckling load. The failure load and shape can be found to observe the path of instability.

2.1.6 Mesh Optimization and Element Selection

The numerical model employs the quadrilateral stress/displacement four-node shell element with reduced integration (S4R), featuring large-strain capabilities, for meshing [55]. This element is depicted in Figure 16.

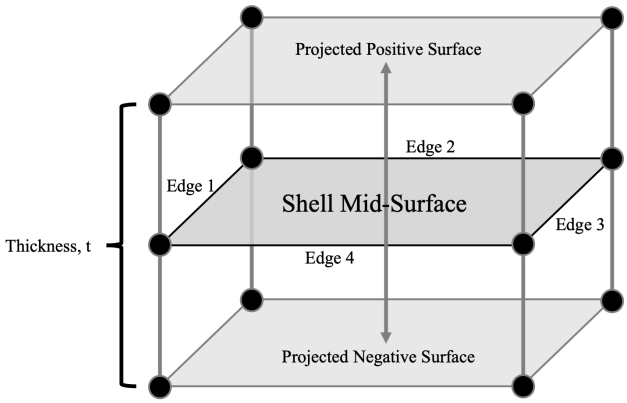

Figure 16: Degenerated mid-surface S4R element.

It approximates the three-dimensional C-section beam as a two-dimensional degenerated mid-surface, streamlining computations without sacrificing accuracy. The S4R element provides six degrees of freedom per node—three translational and three rotational. In ABAQUS, it models the behavior of structures with intrinsic thickness effectively. The mid-surface represents the centroidal plane of the element, with the projected positive and negative surfaces corresponding to the beam's physical boundaries. These projections enable the S4R element to integrate the thickness 't' and mimic the actual structural response without the computational expense of a fully three-dimensional mesh [29]. The validity of this method is supported by research from Gliszczynski and Kubiak [27], as well as Debski and Jonak's use of a similar element, the eight-node shell element with reduced integration (S8R) [30].

When modeling beams with holes, a quad-dominated free meshing strategy is preferred. This technique primarily utilizes quadrilateral elements, introducing triangular elements as needed for complex geometries. It strikes a balance between structured and free meshing methods. An initial mesh size of 5 mm is chosen, as shown in Figure 17.

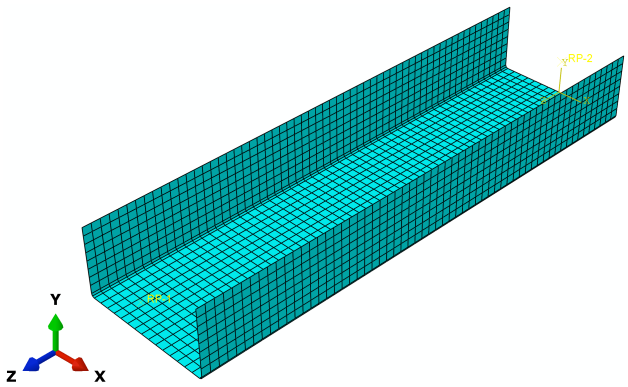

Figure 17: Initial mesh model with 5 mm global seed size.

2.2 Linear Buckling Verification and Validation

Performing an eigenbuckling analysis on a specific layup by conducting a mesh sensitivity analysis ensures that the results are independent of the mesh size, which is critical for obtaining reliable and accurate results. A mesh sensitivity analysis aids in determining the optimal mesh density and checks for buckling mode validation by comparing numerical results with experimental data to ensure that the model accurately captures the critical buckling phenomena before proceeding with the V&V process. Once the eigenbuckling analysis and model iteration have been completed across all five laminate configurations, the next step is to use the Riks method for a more detailed nonlinear analysis of the selected layup.

2.2.1 Model-Experimental Data Validation

Banat and Mania [31] provided the buckling mode shapes for only the C2 configuration; therefore, C2 will be chosen to conduct the analysis with different mesh densities and observe the changes in critical buckling loads and mode shapes. Settle on a mesh size that provides stable results with minimal variation between successive refinements before moving forward with the V&V process.

To perform a mesh sensitivity analysis, a Python script interfacing with ABAQUS was developed [69]. The script extracts desired quantities including model name, buckling loads, and number of elements. Each quantity is then written to a comma-separated value (CSV) file and saved. This data automation ensures a comprehensive validation of all configurations for this study

and facilitates easy implementation of parameters and modularity for subsequent studies.

2.2.2 Mesh Density Sensitivity Analysis

The Python script executed in ABAQUS analyzes mesh sizes from 1 to 5 mm for the C2 configuration, with detailed results in Appendix C.1. A MATLAB script imports the CSV file and generates convergence plots shown in Figure-18, as described in Appendix B.1.

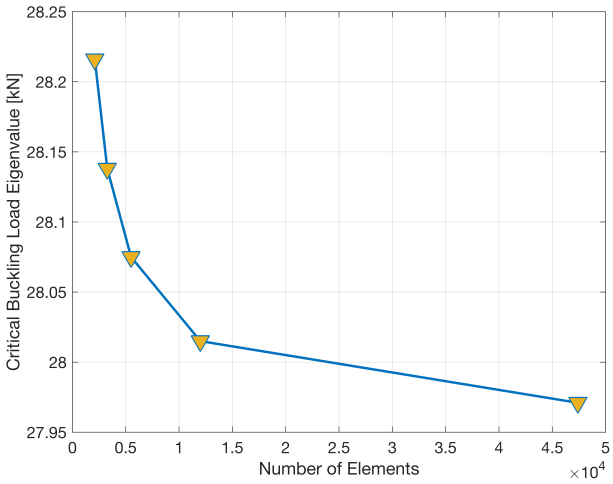

Figure 18: C2 convergence plot.

These plots graph the critical buckling load against the number of elements, illustrating five data points for mesh sizes between 5 and 0.5 mm (from left to right). Figure 18 shows that the C2 configuration demonstrates asymptotic convergence, suggesting an increasing independence of results from mesh size. The convergence table for the C2 C-beam is presented in Table 5, which is processed using the MATLAB code from Appendix B.1 under the 'Convergence Tables' section.

Table 5: Convergence Data for C2

Mesh Size [mm]	Num. of Elements	Eigenvalue [N]	Percent Error [%]
1.0	47400	27971	7.13
2.0	12000	28015	6.98
3.0	5500	28075	6.78
4.0	3268	28138	6.57
5.0	2100	28216	6.31

The MATLAB code section also includes calculations for the percentage error for each simulation, comparing them against the experimental value of 30117 [N] for Banat and Mania's [31] C2 C-beam. The 1 mm mesh fails to accurately capture the physical buckling behavior, as visually supported by Figure 19.

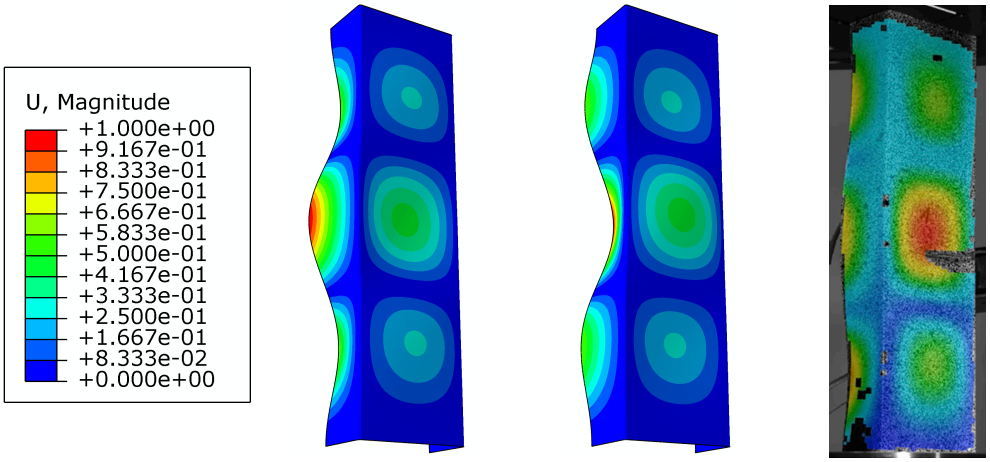

(a) N-M2 (b) N-M1 (c) E [31]

Figure 19: C2 buckling mode shapes with both numerical (N), with mesh sizes of 2 mm (M2) and 1 mm (M1), and experimental (E) results.

The 2 mm mesh closely resembles the experimental buckling modes, underscoring the importance of careful mesh selection. A 1 mm mesh may lead to inaccurate predictions, as evidenced by discrepancies in buckling load predictions. Moreover, a 2 mm mesh falls well within the 10% range of permissible variations between experimental and numerical outcomes in composite structures [27]. Therefore, the study endorses no further refinement beyond 2 mm to enhance the fidelity of the structural response in simulation results, ensuring congruence with experimental observations. This emphasizes the importance of mesh quality in achieving a balance between accuracy in buckling load predictions and guiding the selection of the most efficient mesh size for dependable structural analysis

2.2.3 Model Refinement from Sensitivity Analysis

Building upon the mesh sensitivity analysis, the optimal mesh size is identified as 2 mm, which closely aligns with experimental data both quantitatively and qualitatively, offers a favorable error

margin, and conforms to the established convergence trend. Opting for the 2 mm mesh aligns with the objectives of iterative model refinement. Figure 20 depicts the refined mesh, showcasing this prudent selection.

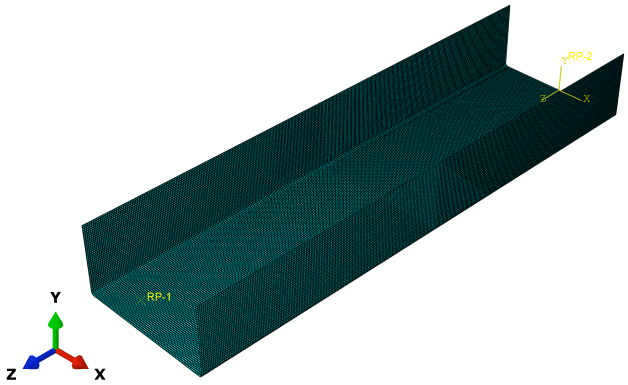

Figure 20: Iterative refinement of the mesh model.

The same Python script was configured to set the mesh size variable to 2 mm and to accept a vector array of string inputs naming the laminate layups from Table 1, C1-C5. The script was then executed in ABAQUS, with results presented in Appendix C.2. These results are tabulated in Table 6, which presents a comparison between the experimental data and the latest iteration of the numerical model for all layups.

Table 6: Comparison of Linear Numerical Model to Experimental Buckling Loads

Model	Critical Buckling Load [N]		Percent Error [%]
	Numerical	Experimental [31]	(Numerical vs Experimental)
C1	28193	31434	10.3
C2	28015	30117	6.98
C3	29308	32634	10.2
C4	28968	30920	6.31
C5	28218	29836	5.42

While the mesh sensitivity analysis contributed to selecting a mesh size that ensured results are independent of the mesh size and validated the buckling mode shape with experimental data, the percentage errors—slightly above 10% for configurations C1 and C3 in Table 6—are outside the acceptable variations between experimental and numerical outcomes [27]. This highlights the limitations of an eigenbuckling analysis in providing a realistic investigation and recreation of

structural performance. These limitations are attributed to assumptions that include small deformations and perfect geometry. The Riks method addresses these assumptions and aids in further achieving more accurate results to meet the acceptable margins for the V&V process.

2.3 Nonlinear Buckling Verification and Validation

Based on the V&V results from the eigenbuckling analysis, the Riks method is used to provide a more comprehensive understanding of post-buckling behavior, including the load-displacement path beyond the initial buckling point. Geometrically nonlinear analyses are introduced here, which account for material nonlinearities such as yielding and failure stress properties listed in Table 2, as well as large deformations. This step is crucial for structures where post-buckling strength or the pathway to failure is as important as the initial buckling load itself. A selected laminate configuration for the C-beam will be simulated, and the buckling load and failure mode will be obtained and verified against experimental results. Once the nonlinear numerical model is verified, a new analysis on more accurate critical buckling loads for all five laminates will be conducted.

2.3.1 Buckling Load Validation

The C2 configuration will be selected and focused on because Banat and Mania [31] provided the failure mode shapes for only that configuration. For V&V, the LPF vs. arc length plot will be extracted which provides important insights into the structural behavior under load. At some point the plot will denote when the structure behaves elastically and is stable up to a certain point. The point where the curve starts to show nonlinearity often corresponds to the onset of buckling [70]. This is where the structure begins to lose stiffness significantly, leading to large deformations for small increases in load [55].

After modifying the ABAQUS eigenbuckling analysis for the C2 configuration to incorporate the Riks method, the CSV file in Appendix C.1 was processed using the MATLAB code in Appendix B.2, which displayed the LPF versus arc length plot in Figure 21.

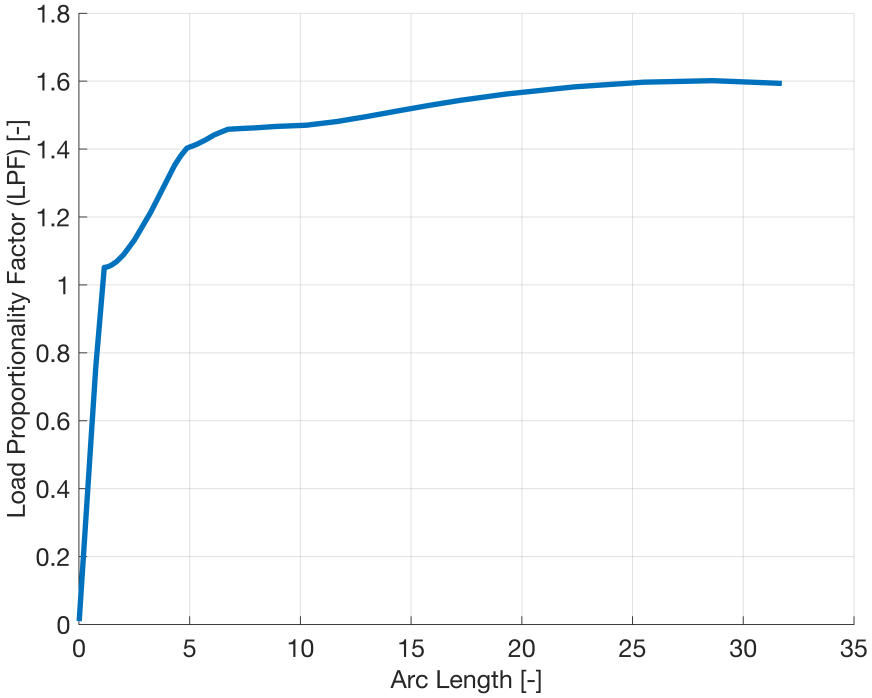

Figure 21: Load proportionality factor (LPF) vs arc length for C2 C-beam

There is a gradual increase in load capacity after an initial buckling point, rather than a sudden drop or jump, which would typically be indicative of snap-through behavior [70]. This suggests that while the structure underwent buckling, it didn't exhibit a snap-through but rather a post-buckling strength increase, where the structure is capable of carrying additional load in a deformed configuration [71]. In many structural systems, particularly in slender structures or shells, once buckling occurs, the structure may still carry additional load but in a different deformation mode [72].

Figure 21 clearly shows where the linear region ends and the structure begins to behave nonlinearly, which is aligned with standard practices in buckling analysis. This transition zone typically represents the critical load beyond which the structure may not return to its original state under unloading, indicating potential buckling or yielding [73, 74]. Therefore, the onset of buckling occurs at a LPF of 1.05157 and an arc length of 1.1433. Taking the eigenbuckling value from Table 6, the new C2 buckling load for the nonlinear analysis is established as follows:

$$P_{cr} = 28015 \text{ N} \times 1.05157 = 29460 \text{ N} \tag{17}$$

As a result, the percentage error between the experimental results and the nonlinear analysis is 2.18%, representing a significant reduction from the 6.98% error observed in the eigenbuckling analysis. This improvement highlights the effectiveness of the Riks method in closely approximating real-world behavior, thereby enhancing the reliability of structural assessments. This accuracy suggests that the numerical model is reasonably precise in predicting experimental behavior, although minor discrepancies can arise from modeling assumptions such as using coupling constraints for simplification instead of applying individual nodes for boundary conditions.

2.3.2 Failure Mode Validation

Figure 21 indicates where the material experiences failure. The failure mode is obtained at an arc length of 31.746, corresponding to an LPF of 1.5934; this is where the negative increments are observed. Taking the C2 eigenbuckling value from Table 6, the C2 failure load for the nonlinear analysis becomes $P_{\text{failure}} = 28015 \times 1.5934 = 44639$ N, which is demonstrated and compared with experimental data in Figure 22.

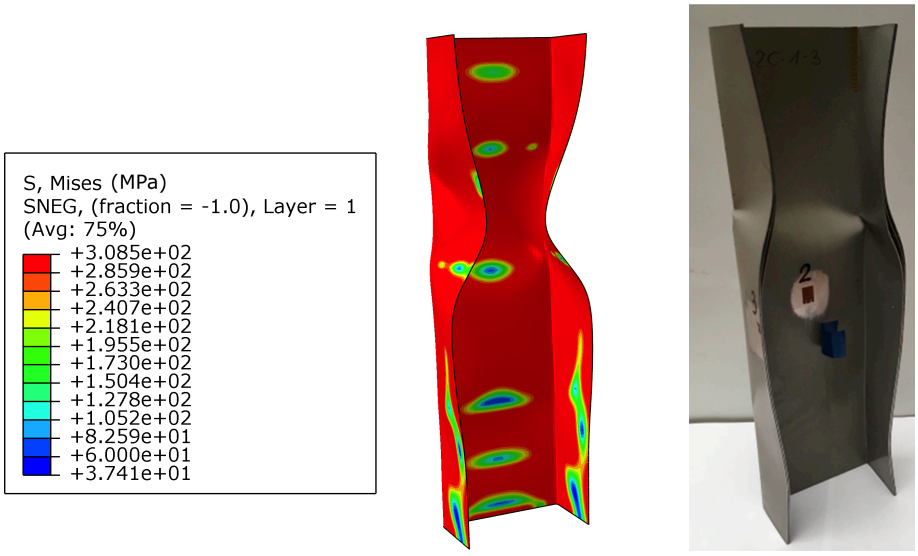

(a) N (b) E [31]

Figure 22: C2 failure mode shapes with both numerical (N) and experimental (E) results.

Figure 22a shows the stress distribution using the von Mises stress criteria in the numerical model, which is commonly used to predict yielding of ductile materials under complex loading [75]. The color coding indicates the stress levels, with red representing the highest at 308.5 MPa, set as R_y for the aluminum layer. This stress distribution aids in identifying potential failure zones, which correspond to the areas of highest stress concentration. The areas in green and blue indicate lower stress levels, suggesting these parts of the structure are less likely to fail under the given load conditions. Figure 22b shows physical deformations and damage of the experimental C-beam, which closely match the high-stress areas predicted by the numerical model in Figure 22. This correlation is significant because it validates the accuracy of the numerical model in predicting how the material will behave under load, particularly in terms of where it will buckle and likely fail. Banat and Mania did not provide failure loads ($P_{failure}$) for the experimental specimen in Figure 22b to compare with numerical values. Now that the C2 configuration has been verified, the new critical buckling loads across all five laminates can be calculated.

2.3.3 Nonlinear vs. Linear Model Buckling Loads

After modifying the ABAQUS eigenbuckling analysis for C1-C5 C-beam configurations to incorporate the Riks method, the CSV files in Appendices C.2 to C.5 were processed using the MATLAB code in Appendix B.3 and compiled into the LPF versus arc length plots in Figure 21.

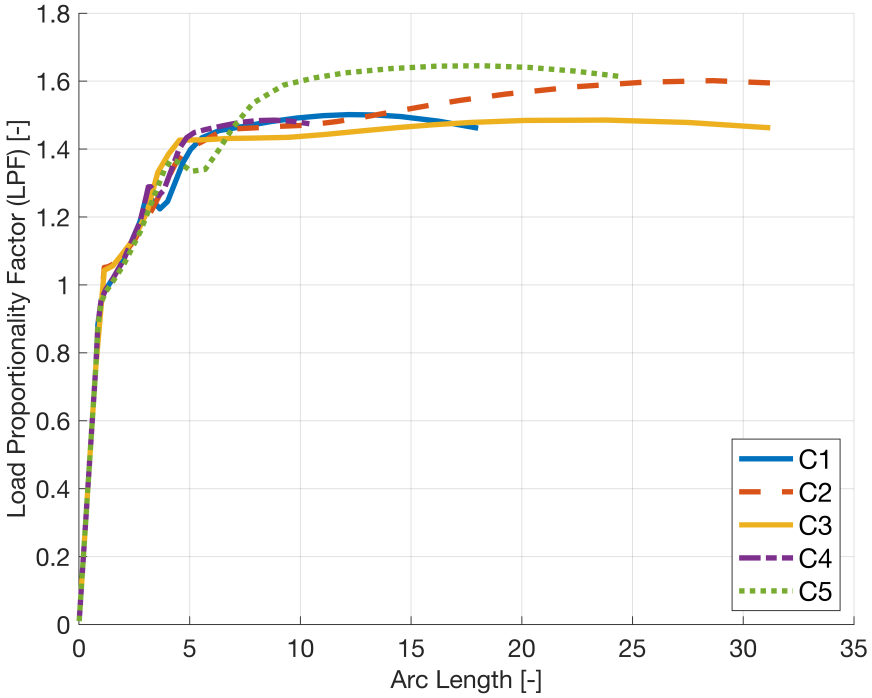

Figure 23: Load proportionality factor (LPF) vs arc length for C1-C5 C-beams.

After obtaining the LPF for each configuration at the onset of buckling and multiplying these values by their respective eigenbuckling values from Table 6, the results for the nonlinear model buckling loads are presented in Table 7.

Table 7: Comparison of Nonlinear Numerical Model to Experimental Buckling Loads

Model	Critical Buckling Load [N]		Percent Error [%]
	Numerical	Experimental [31]	(Numerical vs Experimental)
C1	30324	31434	3.53
C2	29460	30117	2.18
C3	30949	32634	5.16
C4	29530	30920	4.50
C5	28529	29836	4.38

The comparison between linear and nonlinear numerical models, as seen in Tables 6 and 7, demonstrates a significant reduction in percentage error when using the nonlinear model to estimate experimental buckling loads. Specifically, the percentage errors in the linear model range from 5.42% to 10.3%. In contrast, the errors in the nonlinear model are considerably lower, ranging

between 2.18% and 5.16%, and fall well within the 10% range of acceptable variations between experimental and numerical results in composite structures [27]. This reduction in error suggests that the nonlinear model, particularly when employing the Riks method, is more adept at capturing the complex behaviors associated with buckling, including material and geometric nonlinearities that linear analysis does not consider. This capability is crucial for analyzing GLARE materials, where accurate predictions of where aluminum may yield and R-Glass/Epoxy might fail are vital for applications demanding high safety and durability.

Moreover, compared to eigenbuckling assumptions, the Riks method provides a more realistic approximation of buckling loads and additional information on post-buckling behavior [76, 77]. Eigenbuckling analysis typically assumes perfect linearity and small deformations, idealizing the behavior of materials and structures under load [55]. In contrast, the Riks method accounts for the nonlinear load-deformation relationship and can incorporate the effects of large deformations and material yielding [55], which is crucial for materials like GLARE laminates that exhibit complex interactions between their components under stress [78].

Now that the numerical modeling and V&V have been completed for all C1-C5 C-beam configurations, the next chapter will explore ways to enhance both the pre- and post-buckling strength of a GLARE C-beam by examining the effects of adding cross stiffeners.

Chapter 3. Introduction of Cross Stiffeners

This exploration delves into one distinct type of stiffener—cross stiffeners—inspired by the research of Prado et al. on steel I-beams under lateral torsional bending [25]. The aim is to assess the potential of these cross stiffeners to enhance both the pre- and post-buckling strength of GLARE C-beams.

3.1 Modeling

In the modeling phase, integrating cross stiffeners within the C-beam is focused on aligning geometric and material characteristics with mechanical and structural criteria. The process entails detailing assumptions, geometric configurations, and computational strategies critical for simulating interactions between the stiffeners and the C-beam. This comprehensive examination prepares the groundwork for a detailed numerical analysis, which will assess the stiffeners' effectiveness in enhancing both pre- and post-buckling strengths.

3.1.1 Stiffener Geometry and Modeling Assumptions

C2 C-beam configuration is chosen because of the low percent error and the additional experimental buckling and failure loads provided. In this preliminary study, the focus is on establishing a proof-of-concept for the improvement of damage tolerance of GLARE C-beam with introduction of cross stiffeners. While the details of bonding techniques and their effects are crucial for a comprehensive understanding, they are not the primary focus at this stage. Future research can delve into the specifics of bonding methods and their impact on the mechanical properties and performance of the stiffened structures. Drawing upon the geometrical descriptions provided by Prado et al. [25], one set of cross stiffener was modeled and positioned at 61 mm from each C-beam end, where two of the local buckling occured, Figure 19a, and an attempt at redistributing the stresses and helping to prevent such deformations. A clearance of 1.75 mm is maintained between the stiffeners to the web due to the radius fillet. The specific dimensions of the cross stiffener are

illustrated in Figure 24.

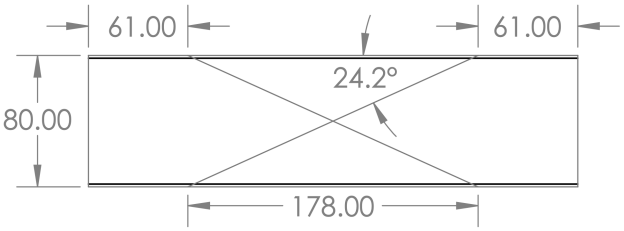

Figure 24: Cross Stiffener dimensions (units in mm).

The dimensions discussed were used to create models of the cross stiffener integrated into the existing C-beam using SOLIDWORKS. This model was then converted to IGS format and imported into ABAQUS to simulate the cross stiffener as part of the beam assembly. The graphical representations of the stiffeners integrated into the beam are exhibited in Figure 24. Figure 25 shows the beam with the stiffeners incorporated, providing a three-dimensional perspective of the placement of the cross stiffener within the C-beam's architecture.

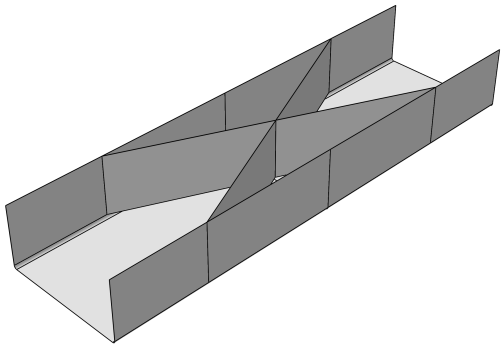

Figure 25: Beam with incorporated stiffeners.

The Python script was modified to import the distinct IGS model, as shown in Figure 25. Each model is associated with unique surface set region definitions that are used for assigning material properties and applying coupling constraints at the beam ends.

3.1.2 Stiffener Material Properties and Coordinate System Definitions

Constructed as GLARE laminates, each stiffener will mirror the material properties of the C-section beam detailed in Section 2.1.2. The mechanical properties, as listed in Table 2, along

with the laminate stacking approach for the stiffeners, will adhere to the modeling principles applied to the beam's web or flange laminates. This ensures methodological consistency, facilitating a unified analysis of composite behavior and enabling direct comparison of structural performance across configurations. This approach not only streamlines the evaluation process but also enhances the reliability of the study's conclusions.

The coordinate systems for each stiffener type must align with the comprehensive composite modeling methodology discussed in Section 2.1.2. Figure 26 shows the layup orientations for the cross stiffener.

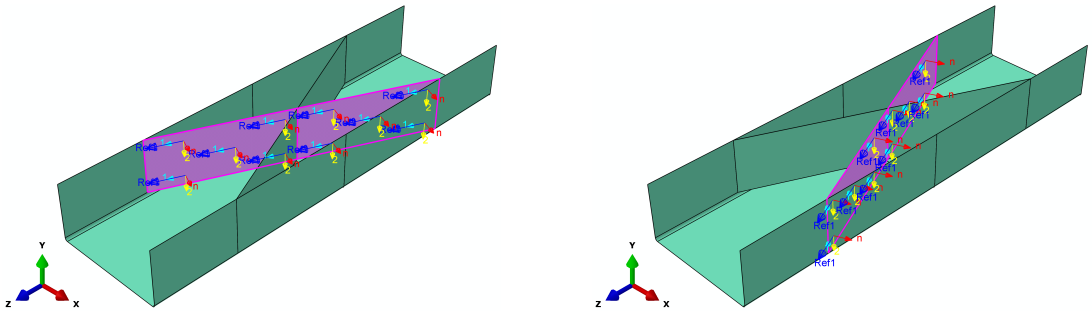

(a) Top left laminates.

(b) Top right laminates.

Figure 26: Fiber orientations at 0° ply for cross stiffeners.

For the cross stiffeners, the top left laminates (Figure 26a) have a normal vector of $(0.9121, 0.0, 0.4099)$ and a primary direction vector of $(-0.4099, 0.0, 0.9121)$, setting the global 3-axis along the global datum z-axis and the global 2-axis along the global datum y-axis. Similarly, for the top right laminates (Figure 26b), the normal vector is $(0.9121, 1.0, -0.4099)$ with the primary direction vector $(0.4099, 0.0, 0.9121)$.

3.2 Results

Executing the modified Python script in ABAQUS for the eigenbuckling analysis yielded a buckling load of 32070 N, as shown in Figure 27.

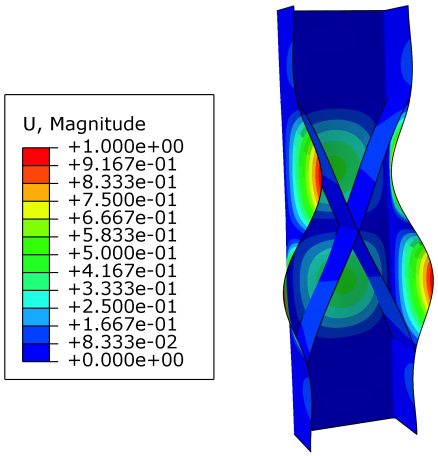

Figure 27: Cross stiffener configuration bucking mode plot.

After the eigenbuckling analysis was modified for the Riks analysis, the failure of the C-beam is shown in Figure 28.

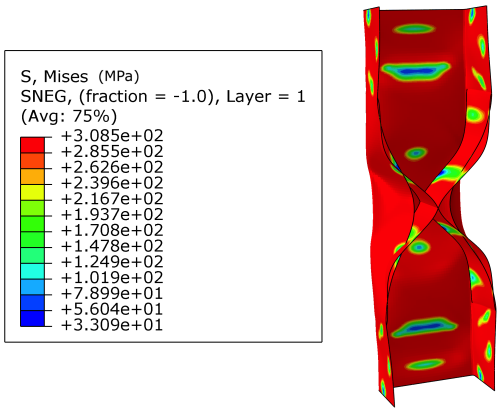

Figure 28: Cross stiffener configuration failure mode plot.

In addition, the LPF vs. arc length data was extracted (Appendix C.6) and plotted together with the C2 configuration without a stiffener (Appendix C.1) using the MATLAB code in Appendix B.4, which produced Figure 29.

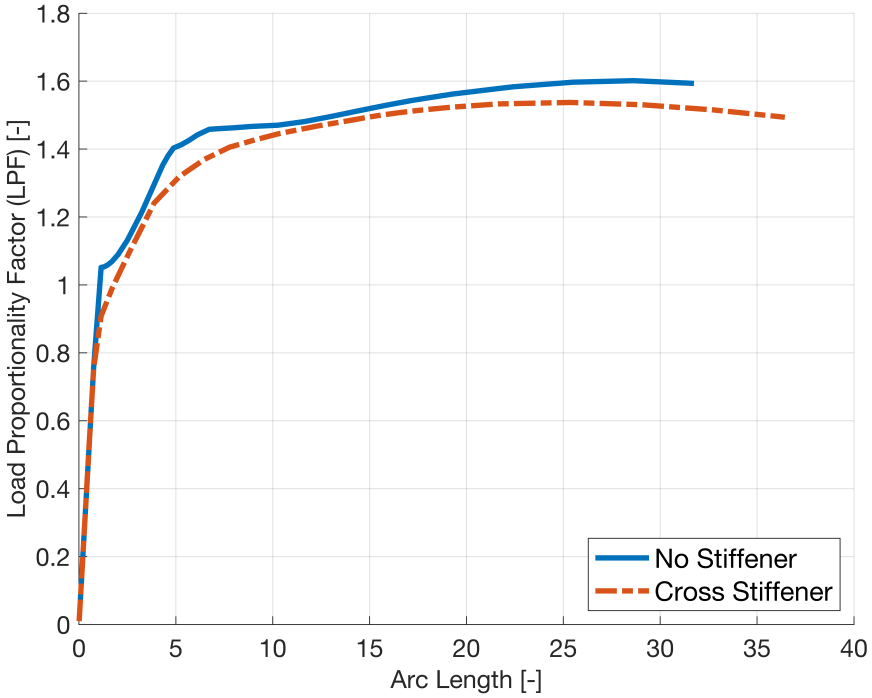

Figure 29: Load proportionality factor (LPF) vs arc length for C2 C-beam with and without cross stiffener

Since non-linearity appears everywhere in the cross configuration, the 0.2% offset method was employed to determine the LPF at the onset of yielding [79]. This method involves identifying the point at which the curve deviates from linearity by 0.2%, indicating the onset of yielding, which corresponds to an LPF of 0.7549. The failure load is obtained at an arc length where negative increments are observed, corresponding to an LPF of 1.49381. The obtained buckling and failure loads for the cross configuration, calculated by multiplying the eigenbuckling load, 28015 N, by the respective LPF values of 1.09447 and 1.49381, are tabulated alongside the configuration without a stiffener in Table 7.

Table 8: Comparison of Nonlinear Numerical Models of Cross and No Stiffener C2 C-beam Buckling Loads

Stiffener	Load [N]	
	Buckling	Failure
Cross	21149	46956
None	29460	30117

For further comparison of the performance between the cross and no-stiffener configurations, in the C2 C-beam, the pre- and post-buckling paths have been plotted using the same data (see Appendices C.1 and C.6) but processed through the MATLAB code in Appendix B.5 resulting in Figure 30.

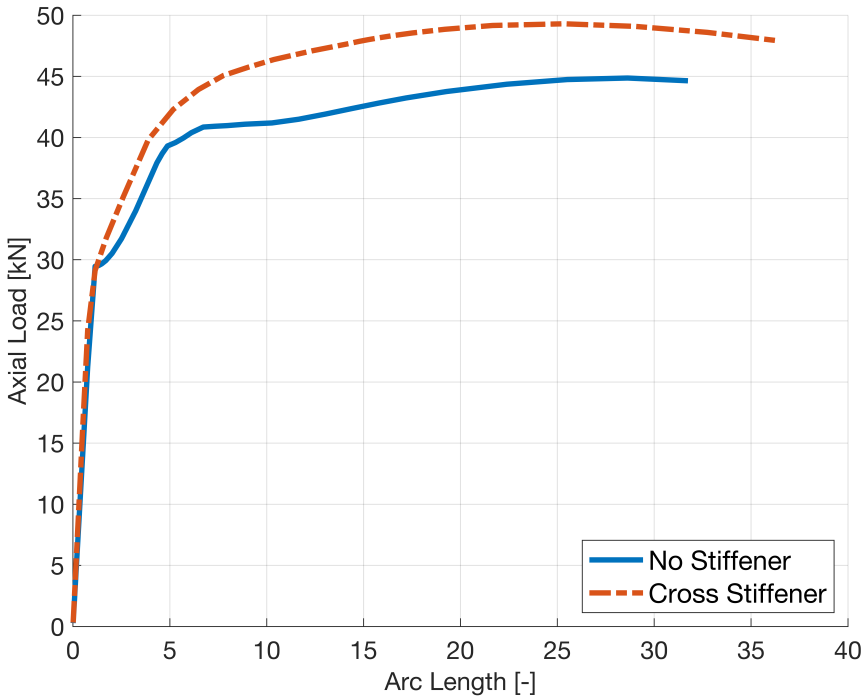

Figure 30: Axial load (kN) vs arc length for C2 C-beam with and without cross stiffener.

In the axial load plot, Figure 27 shows that the deformation of the buckling mode shape is primarily concentrated at the mid-span of the beam, redistributing these stresses at the center. This indicates that the cross stiffeners potentially create crumple zones, which are desirable in crashworthy designs, where buckling and other deformation mechanisms are intended to occur [80]. These zones are designed to buckle early in the impact process, reducing the initial kinetic force involved and protecting the more rigid, occupant-protecting parts of the structure [81]. In contrast, Figure 19a shows significant deformation concentrated in multiple regions along the beam length. Additionally, Table 8 shows a 39% decrease in buckling load from the no-stiffener configuration to the cross-stiffener configuration. The earlier onset of buckling can absorb and dissipate more energy from an impact, making deformation more predictable and controlled [82].

Figure 28 illustrates that the cross stiffeners contribute to a more distributed failure pattern and controlled deformation compared to the no-stiffener configuration in Figure 22, which fails at a lower load with more pronounced localized deformations and stress concentrations. This suggests an improvement in the overall load-carrying capacity and structural integrity of the C-beam. Furthermore, Figure 29 demonstrates that the introduction of cross stiffeners results in a higher and more stable load path factor, indicating improved stability and load-bearing capacity. Additionally, Figure 30 illustrates that the stiffened beam can sustain higher loads, exhibit a more gradual decline after reaching the peak load, and maintain better stability, confirming the beneficial impact of the cross stiffeners. This improvement is further evidenced by Table 8, which records a 36% increase in failure load from the no-stiffener configuration to the cross-stiffener configuration.

To emphasize from Chapter 1, such characteristics are critical for applications that require energy absorption mechanisms and dissipation, particularly in the crashworthiness design of aerospace structures. These include fuel tanks to minimize the risk of fire, subfloors, seats, and airframes that maintain a survivable space during hard landings or collisions, thus protecting occupants and critical components [24, 83].

Chapter 4. Future Directions and Conclusions

This research has established the fundamental impact of incorporating cross stiffeners in GLARE C-beams on their pre- and post-buckling performance. The numerical models validated in this study demonstrate that cross stiffeners significantly enhance the stability of thin-walled composite beams under quasi-static compressive loading, with a 39% decrease in buckling loads and a 36% increase in failure loads from the no-stiffener configuration to the cross-stiffener configuration. These findings are particularly relevant for the aerospace industry, where GLARE materials are favored for their superior fatigue resistance [6], impact resistance [7], strength-to-weight ratio [13], and crashworthiness [16]. The application of cross stiffeners can lead to future studies involving classical impact tests to investigate crashworthy aerospace structures, such as fuselage skins, subfloors, and other critical components. This promising direction sets the stage for a discussion on how GLARE, alongside emerging materials like Polylactic Acid (PLA) and Polyhydroxyalkanoate (PHA), could shape the future of aircraft development, emphasizing sustainability, efficiency, and cutting-edge technological integration.

4.1 Future Research Directions

The journey of material innovation in aerospace engineering continues to evolve, particularly with the introduction of sustainable materials such as PLA and PHA, combined with fiber-reinforced particles like metals to create Metal Matrix Composites (MMCs) [84, 85]. These innovative materials promise to enhance structural performance and contribute to environmental sustainability [86].

A promising research direction involves utilizing these materials in three-dimensional (3D) printing processes. This approach includes determining their mechanical properties using ASTM standards, developing new material models for the stiffeners, and conducting additional pre- and post-buckling analysis to compare their performance with traditional GLARE stiffeners.

To ascertain the mechanical properties of composites, including elastic moduli (E_1, E_2), shear

modulus (G_{12}), and Poisson's ratio (ν), several ASTM standards are applicable. ASTM D638 provides guidelines for tensile testing of plastics, including PLA, to determine E_1 and ν [87]. ASTM D790 outlines methods for assessing the flexural properties of unreinforced and reinforced plastics, thereby determining E_2 [88]. For shear properties, ASTM D5379 offers a standard approach to measure G_{12} [89], and Poisson's ratio can be determined indirectly from the results of tensile and shear tests [90]. These ASTM standards have been used for hybrid composites such as MMCs [91, 92, 93].

The integration of bio-based polymers and fiber-reinforced particles not only offers environmental benefits but also provides the flexibility required for modern manufacturing processes [94, 95], aligning with the aerospace industry's shift towards greener and more sustainable practices [96].

4.2 Concluding Remarks

The research presented in this thesis has demonstrated the significant benefits of incorporating cross stiffeners in GLARE C-beams, highlighting their potential to enhance both pre- and post-buckling strength for crashworthy aerospace structures. The validated numerical models provide a robust framework for further investigation and optimization of composite structures. Future research should continue to explore innovative sustainable materials to fully realize the potential of these findings. The integration of sustainable materials and comprehensive testing will ensure that advancements in structural performance also align with environmental and operational goals.

By pursuing these future directions, the research community can continue to push the boundaries of aerospace structures, shaping the next generation of safer, more efficient, and environmentally responsible aircraft.

References

[1] D. Banat and R. J. Mania, "Damage analysis of thin-walled GLARE members under axial compression – Numerical and experiment investigations," *Composite Structures*, vol. 241, p. 112102, 2020.

[2] M. A. Alam, H. H. Ya, S. M. Sapuan, O. Mamat, B. Parveez, M. Yusuf, F. Masood, and R. A. Ilyas, *Advanced Composites in Aerospace Engineering Applications*, ser. 0925-0042. Dordrecht, Netherlands: Springer Cham, 2022, no. 1.

[3] H. Seo, H. T. Hahn, and J.-M. Yang, "Impact Damage Tolerance and Fatigue Durability of GLARE Laminates," *Journal of Engineering Materials and Technology*, vol. 130, p. 041002, 2017.

[4] N. A. Patil, S. S. Mulik, K. S. Wangikar, and A. P. Kulkarni, "Characterization of Glass Laminate Aluminium Reinforced Epoxy- A Review," *Procedia Manufacturing*, vol. 20, pp. 554–562, 2018.

[5] T. Trzepieciński, S. M. Najm, M. Sbayti, H. Belhadjsalah, M. Szpunar, and H. G. Lemu, "New Advances and Future Possibilities in Forming Technology of Hybrid Metal–Polymer Composites Used in Aerospace Applications," *Journal of Composites Science*, vol. 5, pp. 554–562, 2018.

[6] H. G. Kotik and J. E. P. Ipiña, "Short-beam shear fatigue behavior of fiber metal laminate (Glare)," *International Journal of Fatigue*, vol. 95, pp. 236–242, 2017.

[7] M. M. Kadhim and F. A. Alshamma, "Glass laminate aluminum reinforced epoxy under non-proportional multiaxial fatigue loading: Experimental testing and new fatigue apparatus development," *Results in Engineering*, vol. 20, p. 100773, 2022.

[8] Y. Huang, J. Liu, X. Huang, J. Zhang, and G. Yue, "Delamination and fatigue crack growth

behavior in Fiber Metal Laminates (Glare) under single overloads," *International Journal of Fatigue*, vol. 78, pp. 53–60, 2015.

[9] W. Asghar, M. A. Nasir, F. Qayyum, M. Shah, M. Azeem, S. Nauman, and S. Khushnood, "Investigation of fatigue crack growth rate in CARALL, ARALL and GLARE," *International Journal of Fatigue*, vol. 40, pp. 1086–1100, 2017.

[10] B. Xie, L. Gao, S. Jiang, S. Zhang, C. Wu, and X. Ran, "Notched tensile response and damage mechanism of the GLARE laminate," *Journal of Composite Materials*, vol. 54, pp. 3037–3046, 2020.

[11] F. D. Morinière, R. C. Alderliesten, and R. Benedictus, "Energy distribution in GLARE and 2024-T3 aluminium during low-velocity impact," in *28th International Congress of the Aeronautical Sciences*. Brisbane, Australia: International Council of the Aeronautical Sciences, September 2012, pp. 1–9.

[12] R. Das, A. Chanda, J. Brechou, and A. Banerjee, *Dynamic Deformation, Damage and Fracture in Composite Materials and Structures*. Cambridge, England: Woodhead Publishing, 2023, no. 2.

[13] P. K. D. Kumar, B. Rajendran, B. Subeetsha, and N. Swetha, "Study on tensile, flexural and impact strength of GLARE reinforced with sugarcane bagasse ash microparticles," *Materials Today: Proceedings*, vol. 47, pp. 1059–1064, 2021.

[14] R. Huang, M. Riddle, D. Graziano, J. Warren, S. Das, S. Nimbalkar, J. Cresko, and E. Masanet, "Energy and emissions saving potential of additive manufacturing: the case of lightweight aircraft components," *Journal of Cleaner Production*, vol. 135, pp. 1559–1570, 2016.

[15] H. Mou, J. Xie, Z. Feng, and X. Shi, "Review on the crashworthiness design and evaluation of fuselage structure for occupant survivability," *Progress in Aerospace Sciences*, vol. 135, p. 101001, 2024.

[16] R. Subbaramaiah, B. G. Prusty, G. M. K. Pearce, S. H. Lim, and R. S. Thomson, "Crashworthy response of fibre metal laminate top hat structures," *Composite Structures*, vol. 160, pp. 773–781, 2017.

[17] F. Caputo, G. Lamanna, D. Perfetto, A. Chiariello, F. D. Caprio, and L. D. Palma, "Experimental and Numerical Crashworthiness Study of a Full-Scale Composite Fuselage Section," *AIAA Journal*, vol. 59, 2020.

[18] M. Guida, F. Marulo, and S. Abrate, "Advances in crash dynamics for aircraft safety," *Progress in Aerospace Sciences*, vol. 98, pp. 106–123, 2018.

[19] T. Sinmazçelik, E. Avcu, M. Özgür Bora, and O. Çoban, "A review: Fibre metal laminates, background, bonding types and applied test methods," *Materials & Design*, vol. 32, pp. 3671–3685, 2011.

[20] C. Qi, G. Zhidong, L. Zengshan, J. Zhaojie, and Z. Yue, "Experimental investigation on impact performances of GLARE laminates," *Chinese Journal of Aeronautics*, vol. 28, pp. 1784–1792, 2015.

[21] Y. Chen, J. Yang, X. Qiu, C. Ji, and B. Wang, "DIC-based constant amplitude and two-block loading fatigue life prediction of open hole GLARE laminate," *Engineering Fracture Mechanics*, vol. 278, p. 109016, 2023.

[22] G. S. E. Bikakis, C. D. Dimou, and E. P. Sideridis, "Ballistic impact response of fiber–metal laminates and monolithic metal plates consisting of different aluminum alloys," *Aerospace Science and Technology*, vol. 69, pp. 201–208, 2017.

[23] Y. Zhong and S. C. Joshi, "Response of hygrothermally aged GLARE 4A laminates under static and cyclic loadings," *Materials & Design*, vol. 87, pp. 138–148, 2015.

[24] J.-Q. Yang, T.-Q. Liu, and P. Feng, "Enhancing flange local buckling strength of pultruded GFRP open-section beams," *Composite Structures*, vol. 244, no. 112459, 2020.

[25] N. I. Prado, J. Carrillo, G. A. Ospina, and D. Ramirez-Amaya, "Experimental assessment of I-shaped steel beams with longitudinal stiffeners under lateral-torsional buckling," *DNYA*, vol. 85, no. 207, 2018.

[26] S. Guo, D. Li, X. Zhang, and J. Xiang, "Buckling and post-buckling of a composite C-section with cutout and flange reinforcement," *Composites: Part B*, vol. 60, pp. 119–124, 2014.

[27] A. Gliszczynski and T. Kubiak, "Progressive failure analysis of thin-walled composite columns subjected to uniaxial compression," *Composite Structures*, vol. 169, pp. 52–61, 2017.

[28] A. Gliszczynski, T. Kubiak, and L. Borkowski, "Experimental investigation of pre-damaged thin-walled channel section column subjected to compression," *Composites: Part B*, vol. 147, pp. 56–68, 2018.

[29] H. Debski, A. G. P. Rozylo, and T. Kubiak, "Numerical models for buckling, postbuckling and failure analysis of pre- damaged thin-walled composite struts subjected to uniform compression," *Thin-Walled Structures*, vol. 139, pp. 53–65, 2019.

[30] H. Debski and J. Jonak, "Failure analysis of thin-walled composite channel section columns," *Composite Structures*, vol. 132, pp. 567–574, 2015.

[31] D. Banat, Z. Kolakowski, and R. J. Mania, "Investigations of fml profile buckling and post-buckling behaviour under axial compression," *Thin-Walled Structures*, vol. 107, pp. 335–344, 2017.

[32] D. Banat, R. J. Mania, and R. Degenhardt, "Stress state failure analysis of thin-walled GLARE composite members subjected to axial loading in the post-buckling range," *Composite Structures*, vol. 289, p. 115468, 2022.

[33] R. J. Mania and C. B. York, "Buckling strength improvements for Fibre Metal Laminates using thin-ply tailoring," *Composite Structures*, vol. 159, pp. 424–432, 2017.

[34] M. Zaczynska and R. J. Mania, "Investigation of dynamic buckling of fiber metal laminate thin-walled columns under axial compression," *Composite Structures*, vol. 271, p. 114155, 2021.

[35] R. F. Gibson, *Shigley's Mechanical Engineering Design*, ser. 0925-0042. New York, New York: McGraw-Hill Education, 2020, no. 11.

[36] Z. Huang, X. Dai, and L. Dong, "Buckling failures of reserved thin pillars under the combined action of in-plane and lateral hydrostatic compressive forces," *Computers and Geotechnics*, vol. 87, pp. 128–138, 2017.

[37] M. Abouhamzeh, J. Sinke, K. M. B. Jansen, and R. Benedictus, "Thermo-viscoelastic analysis of GLARE," *Composites Part B: Engineering*, vol. 99, pp. 1–8, 2016.

[38] B. Müller, S. T. D. Freitas, and J. Sinke, "Measuring thermal diffusion in fiber metal laminates," in *25th International Conference on Adaptive Structures and Technologies*. The Hague, Netherlands: Delft University of Technology, October 2012, pp. 1–9.

[39] S. Mortazavian and A. Fatemi, "Effects of fiber orientation and anisotropy on tensile strength and elastic modulus of short fiber reinforced polymer composites," *Composites Part B: Engineering*, vol. 72, pp. 116–129, 2015.

[40] M. A. Karataş and H. Gökkaya, "A review on machinability of carbon fiber reinforced polymer (CFRP) and glass fiber reinforced polymer (GFRP) composite materials," *Defence Technology*, vol. 14, pp. 318–326, 2018.

[41] R. F. Gibson, *Principles of Composite Material Mechanics*, ser. 0925-0042. Boca Raton, Florida: CRC Press, 2016, no. 4.

[42] M. Agarwal, P. Pasupathy, X. Wu, S. S. Recchia, and A. A. Pelegri, "Multiscale Computational and Artificial Intelligence Models of Linear and Nonlinear Composites: A Review," *Small Science*, vol. 4, p. 2300185, 2024.

[43] A. Dabbagh, A. Rastgoo, and F. Ebrahimi, "Finite element vibration analysis of multi-scale hybrid nanocomposite beams via a refined beam theory," *Thin-Walled Structures*, vol. 140, pp. 304–317, 2019.

[44] R. Grytz, K. Krishnan, R. Whitley, V. Libertiaux, I. A. Sigal, C. A. Girkin, and J. C. Downs, "A mesh-free approach to incorporate complex anisotropic and heterogeneous material properties into eye-specific finite element models," *Computer Methods in Applied Mechanics and Engineering*, vol. 358, p. 112654, 2020.

[45] Computers and Structures, Inc., "Eigenvalue vs. nonlinear buckling analysis," 2024, [Online; accessed 26-April-2024]. [Online]. Available: https://wiki.csiamerica.com/display/kb/Eigenvalue+vs.+Nonlinear+buckling+analysis

[46] J. Xu, Q. Zhao, and P. Qiao, "A Critical Review on Buckling and Post-Buckling Analysis of Composite Structures," *Frontiers in Aerospace Engineering*, vol. 41, pp. 249–280, 2013.

[47] G. Zucco and P. M. Weaver, "The role of symmetry in the post-buckling behaviour of structures," *Computer Methods in Applied Mechanics and Engineering*, vol. 476, 2020.

[48] O. Giraldo-Londoño, J. S. Monsalve-Giraldo, and J. D. Aristizabal-Ochoa, "Large-deflection and postbuckling of beam-columns with non-linear semi-rigid connections including shear and axial effects," *International Journal of Non-Linear Mechanics*, vol. 77, pp. 85–95, 2015.

[49] C. Yu, P. Hoogenboom, and J. Rots, "Extension of incremental sequentially linear analysis to geometrical non-linearity with indirect displacement control," *Reviews of Adhesion and Adhesives*, vol. 229, p. 111562, 2021.

[50] C. Zhang and K. T. Tan, "Experimental and numerical investigation of large-scale effect on buckling and post-buckling behavior of tubular structures," *Thin-Walled Structures*, vol. 186, p. 110708, 2023.

[51] X. Liu, C. Bai, X. Xi, S. Zhou, X. Zhang, X. Li, Y. Ren, J. Yang, and X. Yang, "Impact response and crashworthy design of composite fuselage structures: An overview," *Progress in Aerospace Sciences*, p. 101002, 2024.

[52] N. S. Ha and G. Lu, "Thin-walled corrugated structures: A review of crashworthiness designs and energy absorption characteristics," *Thin-Walled Structures*, vol. 157, p. 106995, 2020.

[53] M. M. Shokrieh and S. Akbari, *5 - Measuring residual stresses in composite materials using the slitting/crack compliance method*. Sawston, United Kingdom: Woodhead Publishing, 2021, no. 1.

[54] F. Buiochi and M. A. B. Andrade, "2.04 - Ultrasonic Characterization of Anisotropic Materials," *Materials Science and Materials Engineering*, vol. 2, pp. 65–81, 2014.

[55] Dassault Systèmes Simulia Corp., *ABAQUS Analysis User's Manual*, 6th ed., 2009, accessed: 2024-01-14. [Online]. Available: https://classes.engineering.wustl.edu/2009/spring/mase5513/abaqus/docs/v6.6/index.html

[56] M. Kamocka, M. Zglinicki, and R. J. Mania, "Multi-method approach for FML mechanical properties prediction," *Composites: Part B*, vol. 91, pp. 135–143, 2016.

[57] Q. H. Doan, D.-K. Thai, and N. L. Tran, "A numerical study of the effect of component dimensions on the critical buckling load of a GFRP composite strut under uniaxial compression," *materials*, vol. 13, p. 4, 2020.

[58] M. N. B. Kamarudin, J. S. M. Ali, A. Aabid, and Y. E. Ibrahim, "Buckling Analysis of a Thin-Walled Structure Using Finite Element Method and Design of Experiments," *Aerospace*, vol. 147, no. 10, 2022.

[59] F. M. A. Silva, R. M. Soares, Z. G. N. del Prado, and P. B. Gonçalves, "Intra-well and cross-well chaos in membranes and shells liable to buckling," *Thin-Walled Structures*, vol. 102, p. 877–906, 2020.

[60] S. Fialko and V. Karpilovskyi, "Block subspace projection preconditioned conjugate gradient method in modal structural analysis," *Computers & Mathematics with Applications*, vol. 79, pp. 3410–3428, 2020.

[61] T. Zhang, P. Wang, J. Fu, S. Wang, and C. Lian, "Parallel neural network feature extraction method for predicting buckling load of composite stiffened panels," *Thin-Walled Structures*, vol. 199, p. 111797, 2024.

[62] J. A. C. Ambrosio, *Crashworthiness*, ser. 0254-1971. Vienna, Austria: Springer Vienna, 2014, no. 1.

[63] X.-R. Wang, Q.-G. Rong, S.-L. Sun, and H. Wang, "Stability analysis of slope in strain-softening soils using local arc-length solution scheme," *Journal of Mountain Science*, vol. 14, p. 175–187, 2017.

[64] R. Liu, H. Xiong, X. Wu, and S. Yan, "Numerical studies on global buckling of subsea pipelines," *International Journal of Mechanical Sciences*, vol. 78, pp. 62–72, 2014.

[65] N.-H. Kim, *Nonlinear Finite Element Analysis Procedure*. New York, New York: Springer, 2017, no. 1.

[66] C. Li, H.-S. Shen, and H. Wang, "Thermal post-buckling of sandwich beams with functionally graded negative poisson's ratio honeycomb core," *International Journal of Mechanical Sciences*, vol. 152, pp. 289–297, 2019.

[67] M. Bashir-Ahmed and S. Xiao-Zu, "Arc-length technique for nonlinear finite element analysis," *Applied Physics & Engineering*, vol. 5, p. 618–628, 2004.

[68] S. Benson, J. Downes, and R. S. Dow, "Overall buckling of lightweight stiffened panels using an adapted orthotropic plate method," *Engineering Structures*, vol. 85, pp. 107–117, 2014.

[69] M. Taylor, "MECH 151/251: Finite Element Theory and Applications," Santa Clara University, Department of Mechanical Engineering, 2021.

[70] N. Vasios, "Nonlinear analysis of structures," 2015, accessed: 11-May-2024. [Online]. Available: https://scholar.harvard.edu/sites/scholar.harvard.edu/files/vasios/files/ArcLength.pdf

[71] Y. Feng, H. Zhang, X. Tan, Y. He, T. An, and J. Zheng, "Yielding and lateral torsional buckling limit states for butterfly-shaped shear links," *Composite Structures*, vol. 155, pp. 184–196, 2016.

[72] S. Emam and W. Lacarbonara, "A review on buckling and postbuckling of thin elastic beams," *Composite Structures*, vol. 92, p. 104449, 2022.

[73] A. Farzampour and M. R. Eatherton, "Yielding and lateral torsional buckling limit states for butterfly-shaped shear links," *Engineering Structures*, vol. 180, pp. 442–451, 2019.

[74] Y. Chen and L. Jin, "Reusable Energy-Absorbing Architected Materials Harnessing Snapping-Back Buckling of Wide Hyperelastic Columns," *Advanced Functional Materials*, vol. 31, 2021.

[75] P. D. Barsanescu and A. M. Comanici, "von mises hypothesis revised," *Acta Mechanica*, vol. 228, p. 433–446, 2017.

[76] G.-M. Luo and Y.-C. Hsu, "Nonlinear buckling strength of out-of-roundness pressure hull," *Thin-Walled Structures*, vol. 130, pp. 424–434, 2018.

[77] V. Sengar, M. Nynaru, G. Watts, R. Kumar, and S. Singh, "Postbuckled vibration behaviour of skew sandwich plates with metal foam core under arbitrary edge compressive loads using isogeometric approach," *Thin-Walled Structures*, vol. 184, p. 110524, 2023.

[78] P. Soltani, M. Keikhosravy, R. H. Oskouei, and C. Soutis, "Studying the Tensile Behaviour of GLARE Laminates: A Finite Element Modelling Approach," *Thin-Walled Structures*, vol. 18, p. 271–282, 2011.

[79] J. A. Benito, R. Cobo, W. Lei, J. Calvo, and J. M. Cabrera, "Stress–strain response and microstructural evolution of a FeMnCAl TWIP steel during tension–compression tests," *Materials Science and Engineering: A*, vol. 655, pp. 310–320, 2016.

[80] D. Kenyon, Y. Shu, X. Fan, S. Reddy, G. Dong, and A. J. Lew, "Parametric design of multi-cell thin-walled structures for improved crashworthiness with stable progressive buckling mode," *Thin-Walled Structures*, vol. 131, pp. 76–87, 2018.

[81] S. Bhutada and M. D. Goel, "Crashworthiness parameters and their improvement using tubes as an energy absorbing structure: an overview," *International Journal of Crashworthiness*, vol. 27, pp. 1569–1600, 2022.

[82] N. A. Z. Abdullah, M. S. M. Sani, M. S. Salwani, and N. A. Husain, "A review on crashworthiness studies of crash box structure," *Thin-Walled Structures*, vol. 153, p. 106795, 2020.

[83] Y. Ren and J. Xiang, "Energy absorption structures design of civil aircraft to improve crashworthiness," *The Aeronautical Journal*, vol. 118, pp. 383–398, 2016.

[84] G. Tedla and K. Rogers, "Characterization of 3D printing filaments containing metal additives and their particulate emissions," *Science of The Total Environment*, vol. 875, p. 162648, 2023.

[85] S. Chen, X. Dai, D. Yang, L. Dai, and Y. Hua, "Enhancing PHA production through metal-organic frameworks: Mechanisms involving superproton transport and bacterial metabolic pathways," *Applied Energy*, vol. 348, p. 121571, 2023.

[86] A. Patti, A. Patti, A. Latteri, C. Tosto, E. Pergolizzi, G. Recca, G. Recca, and G. Recca, "Influence of the Processing Conditions on the Mechanical Performance of Sustainable Bio-Based PLA Compounds," *Polymers*, vol. 12, p. 2197, 2023.

[87] "ASTM D638-14, standard test method for tensile properties of plastics," https://www.astm.org/d0638-14.html, ASTM International, 2014, accessed: 2024-04-12.

[88] "ASTM D790-17, standard test methods for flexural properties of unreinforced and reinforced plastics and electrical insulating materials," https://www.astm.org/d0790-17.html, ASTM International, 2017, accessed: 2024-04-12.

[89] "ASTM D5379/D5379M-19e01, standard test method for shear properties of composite materials by the v-notched beam method," https://www.astm.org/d5379_d5379m-19e01.html, ASTM International, 2019, accessed: 2024-04-12.

[90] N. Novak, O. Duncan, T. Allen, A. Alderson, M. Vesenjak, and Z. Ren, "Shear modulus of conventional and auxetic open-cell foam," *Mechanics of Materials*, vol. 157, p. 103818, 2021.

[91] P. S. Shreyas, S. Shriramkumar, R. Sruthisagar, B. V. Ramnath, and C. Elanchezhian, "Studies on Mechanical Behaviour of Aluminium-Silicon Carbide-Copper Metal Matrix Composite," *MATEC Web of Conferences*, vol. 166, 2018.

[92] N. T. Hegde, D. Pai, and R. Hegde, "Heat treatment and mechanical characterization of LM-25/tungsten carbide metal matrix composites," *Materials Today: Proceedings*, vol. 19, pp. 810–817, 2019, 1st International Conference on Manufacturing, Material Science and Engineering.

[93] S. K. Mishra and A. Satapathy, "Ceramic particulate filled ZA-27 metal matrix composites: Comparative analysis," *Materials Science and Technology*, vol. 30, 2014.

[94] J. J. Andrew and H. N. Dhakal, "Sustainable biobased composites for advanced applications: recent trends and future opportunities – A critical review," *Composites Part C: Open Access*, vol. 7, p. 100220, 2022.

[95] D. Carvalho, N. Ferreira, B. França, R. Marques, M. Silva, S. Silva, E. Silva, D. Macário, L. Barroso, C. J. Silva, and C. Oliveira, "Advancing sustainability in the automotive industry: Biopreprегs and fully bio-based composites," *Composites Part C: Open Access*, vol. 14, p. 100459, 2024.

[96] D. Ray, *11 - Green materials for aerospace industries*. Cambridge, England: Woodhead Publishing, 2017, no. 1.

[97] B. S. Bedenik and C. B. Besan, *5 - Basic concepts of structural analysi*. Sawston, United Kingdom: Woodhead Publishing, 1999, no. 1.

[98] H. Anton and A. Kaul, *Elementary Linear Algebra*. Hoboken, New Jersey: Wiley, 2019, no. 12.

Appendix A. Fundamental Approach to Mathematical Foundations of Stress in Orthotropic Composite Materials

The appendix presents a suite of mathematical foundations vital to the understanding of stress in orthotropic composite materials. This compendium is largely informed by the seminal work of Ronald F. Gibson, as articulated in *Principles of Composite Material Mechanics* [41]. Gibson's comprehensive exploration of stress-strain relationships, symmetry in material properties, and the behaviors of composite laminae under various conditions, provides the crucial theoretical underpinning for the numerical modeling techniques employed in this thesis. The concepts distilled herein are applied to extend the grasp of the complex interactions within composite structures, enabling a more profound and precise engineering analysis.

A.1 Mathematical 3D State of Stress General Representation of Anisotropic Lamina

A comprehensive three-dimensional (3D) stress state at a specific point within a material can be characterized by nine stress components σ_{ij} (where $i, j = 1, 2, 3$), as depicted in Figure A1.

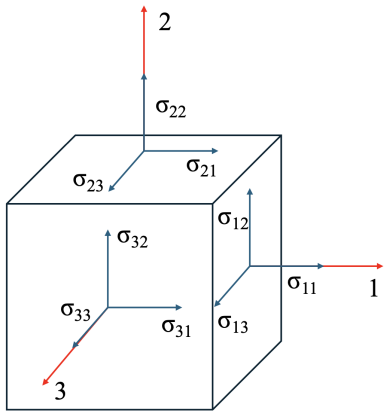

Figure A1: Stress state in three dimensions.

In standard subscript notation, σ_{ij} represents a normal stress when $i = j$; and a shear stress when $i \neq j$. The first subscript indicates the direction of the outward normal to the face where the stress component acts, and the second subscript indicates the direction of the stress component itself.

The generalized Hooke's law, correlating stress components with all nine strain components within an elastic material, is expressed in contracted notation as

$$\sigma_i = C_{ij}\epsilon_j, \quad i, j = 1, 2, \ldots, 6 \tag{A1}$$

Summation is implied over the repeated subscript j. The relationship can be presented in matrix form as

$$\{\sigma\} = [C]\{\varepsilon\} \tag{A2}$$

Here, the elastic constant matrix or stiffness matrix $[C]$ is a 6×6 matrix comprising 36 components, with the stress and strain represented as six-element column vectors. Similarly, the strains can be related to stresses by

$$\epsilon_i = S_{ij}\sigma_j, \quad i, j = 1, 2, \ldots, 6 \tag{A3}$$

and in matrix notation,

$$\{\varepsilon\} = [S]\{\sigma\} \tag{A4}$$

where $[S]$ is the compliance matrix, the inverse of the stiffness matrix $[C]$. The stiffness and compliance matrices are symmetric due to the strain energy density, reflecting mechanical properties of the material. All real materials exhibit a degree of inherent symmetry, which influences their anisotropic behavior, dictated by their atomic and molecular structure.

A.2 Mathematical 3D State of Stress General Representation of Othotropic Lamina

The symmetry within the material's properties enables simplification of the anisotropic Hooke's law. For orthotropic materials, such symmetry allows for two reductions of the generalized model.

A.2.1 First Symmetry Condition

The initial symmetry condition arises from the strain energy density function W, which depends on the strain components ε_i, and is given by

$$W = \frac{1}{2}\varepsilon_i C_{ij} \varepsilon_j \tag{A5}$$

Stress components σ_i are obtained by differentiating W with respect to the strain components:

$$\sigma_i = \frac{\partial W}{\partial \varepsilon_i} = C_{ij}\varepsilon_j \tag{A6}$$

Taking the second derivative of W, one can deduce:

$$\frac{\partial^2 W}{\partial \varepsilon_i \partial \varepsilon_j} = C_{ij} \tag{A7}$$

The symmetry of second derivatives, based on the Maxwell-Betti reciprocity theorem [97], indicates that

$$\frac{\partial^2 W}{\partial \varepsilon_j \partial \varepsilon_i} = C_{ji} \tag{A8}$$

Because the order of differentiation does not affect the outcome (the mixed partial derivatives are equal due to the symmetry of second derivatives), and therefore,

$$\frac{\partial^2 W}{\partial \varepsilon_i \partial \varepsilon_j} = \frac{\partial^2 W}{\partial \varepsilon_j \partial \varepsilon_i} \tag{A9}$$

This results in the stiffness matrix being symmetric ($C_{ij} = C_{ji}$):

$$C_{ij} = \begin{bmatrix} C_{11} & C_{12} & C_{13} & C_{14} & C_{15} & C_{16} \\ & C_{22} & C_{23} & C_{24} & C_{25} & C_{26} \\ & & C_{33} & C_{34} & C_{35} & C_{36} \\ & & & C_{44} & C_{45} & C_{46} \\ & SYM & & & C_{55} & C_{56} \\ & & & & & C_{66} \end{bmatrix} \tag{A10}$$

Considering a full 3D stress state aligned with the principal material axes (refer to Figure A1) and incorporating the symmetric stiffness matrix from Equation A10 into Equation A2, the stress-strain relationship can be expressed as:

$$\begin{Bmatrix} \sigma_1 \\ \sigma_2 \\ \sigma_3 \\ \tau_{23} \\ \tau_{31} \\ \tau_{12} \end{Bmatrix} = \begin{bmatrix} C_{11} & C_{12} & C_{13} & C_{14} & C_{15} & C_{16} \\ & C_{22} & C_{23} & C_{24} & C_{25} & C_{26} \\ & & C_{33} & C_{34} & C_{35} & C_{36} \\ & & & C_{44} & C_{45} & C_{46} \\ & SYM & & & C_{55} & C_{56} \\ & & & & & C_{66} \end{bmatrix} \begin{Bmatrix} \epsilon_1 \\ \epsilon_2 \\ \epsilon_3 \\ \gamma_{23} \\ \gamma_{31} \\ \gamma_{12} \end{Bmatrix} \tag{A11}$$

A.2.2 Second Symmetry Condition

The second symmetry condition in orthotropic materials concerns the invariance of material properties within the 2-3 plane. This symmetry condition influences the configuration of the stiffness matrix, ensuring the properties in the 2 and 3 directions are identical, thereby simplifying the stiffness matrix. As a consequence, the number of independent constants in the stiffness matrix is reduced from the possible thirty-six for a general anisotropic material to nine for an orthotropic material. This reduction is attributable to the material's symmetry, ensuring that $C_{ij} = C_{ji}$, resulting in:

$$C_{ij} = \begin{bmatrix} C_{11} & C_{12} & C_{13} & 0 & 0 & 0 \\ & C_{22} & C_{23} & 0 & 0 & 0 \\ & & C_{33} & 0 & 0 & 0 \\ & & & C_{44} & 0 & 0 \\ & SYM & & & C_{55} & 0 \\ & & & & & C_{66} \end{bmatrix} \tag{A12}$$

This final reduction is a consequence of special orthotropic symmetry. When integrated into Equation A2, the updated stress-strain relationship can be expressed as:

$$\begin{Bmatrix} \sigma_1 \\ \sigma_2 \\ \sigma_3 \\ \tau_{23} \\ \tau_{31} \\ \tau_{12} \end{Bmatrix} = \begin{bmatrix} C_{11} & C_{12} & C_{13} & 0 & 0 & 0 \\ & C_{22} & C_{23} & 0 & 0 & 0 \\ & & C_{33} & 0 & 0 & 0 \\ & & & C_{44} & 0 & 0 \\ & SYM & & & C_{55} & 0 \\ & & & & & C_{66} \end{bmatrix} \begin{Bmatrix} \epsilon_1 \\ \epsilon_2 \\ \epsilon_3 \\ \gamma_{23} \\ \gamma_{31} \\ \gamma_{12} \end{Bmatrix} \tag{A13}$$

Re-expressing in terms of Equation A4:

$$\begin{Bmatrix} \epsilon_1 \\ \epsilon_2 \\ \epsilon_3 \\ \gamma_{23} \\ \gamma_{31} \\ \gamma_{12} \end{Bmatrix} = \begin{bmatrix} S_{11} & S_{12} & S_{13} & 0 & 0 & 0 \\ & S_{22} & S_{23} & 0 & 0 & 0 \\ & & S_{33} & 0 & 0 & 0 \\ & & & S_{44} & 0 & 0 \\ & SYM & & & S_{55} & 0 \\ & & & & & S_{66} \end{bmatrix} \begin{Bmatrix} \sigma_1 \\ \sigma_2 \\ \sigma_3 \\ \tau_{23} \\ \tau_{31} \\ \tau_{12} \end{Bmatrix} \tag{A14}$$

Figures A2 and A3 illustrate the principal and non-principal coordinate systems of an orthotropic lamina, and a material with special orthotropic properties, respectively.

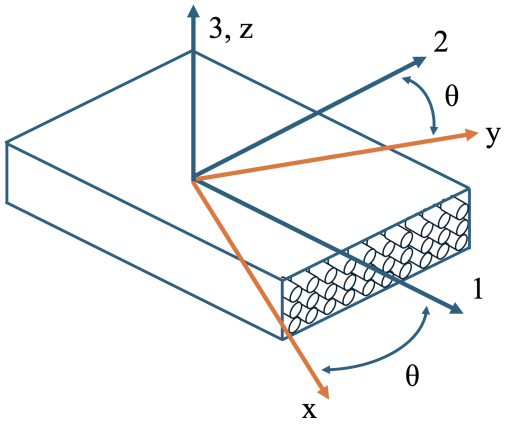

Figure A2: Lamina with orthotropic properties in principal (123) and non-principal (xyz) coordinate systems.

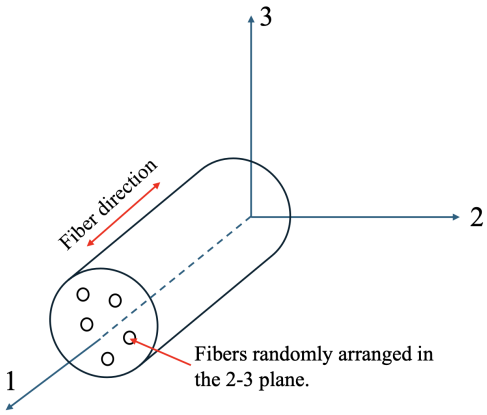

Figure A3: Material with special orthotropic properties and transverse isotropy, demonstrating the 2-3 plane symmetry. [41]

A.3 Mathematical 2D State of Stress Representation of Orthotropic Lamina in Using Engineering Coefficients

Orthotropic lamina is commonly assumed to experience a simplified two-dimensional stress state, also known as plane stress shown in Figure A4.

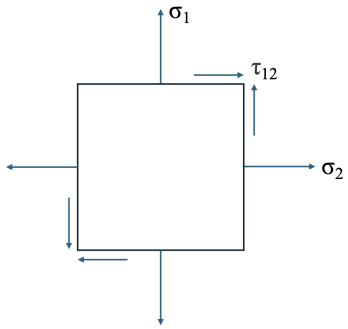

Figure A4: Stress state in two dimensions.

Reducing the dimensionality of the stiffness matrix (Equation A14) from 3D to 2D eliminates all terms containing a 3-direction component ($\sigma_3 = \tau_{23} = \tau_{31} = 0$), leading to the following transformation:

$$\begin{Bmatrix} \epsilon_1 \\ \epsilon_2 \\ \gamma_{12} \end{Bmatrix} = \begin{bmatrix} S_{11} & S_{12} & 0 \\ S_{21} & S_{22} & 0 \\ 0 & 0 & S_{66} \end{bmatrix} \begin{Bmatrix} \sigma_1 \\ \sigma_2 \\ \tau_{12} \end{Bmatrix} = [S] \begin{Bmatrix} \sigma_1 \\ \sigma_2 \\ \tau_{12} \end{Bmatrix} \tag{A15}$$

A.3.1 Deriving the Connection between Engineering Coefficients and Terms in the Compliance Matrix

Orthotropic materials are characterized by unique directional properties, necessitating the use of subscripts on engineering constants to denote directional dependency. Unlike isotropic materials, where properties such as Young's modulus and Poisson's ratio are uniform in all directions, orthotropic materials exhibit distinct values in different directions, such that $E_1 \neq E_2$ and $\nu_{12} \neq \nu_{21}$. For isotropic materials, a negative sign in the definition of Poisson's ratios is common, but separate definitions are necessary for orthotropic materials. The major Poisson's ratio, typically denoted as ν_{12}, describes the ratio of the transverse strain to the axial strain in the material's primary direction, while the minor Poisson's ratio, ν_{21}, defines this relationship in the transverse direction. In the principal material coordinate system, a normal stress induces only normal strains, with all shear strains being null, indicating no shear-normal interaction. The orthotropic material properties for

the plane stress case are derived using three loading conditions shown in Figure A5.

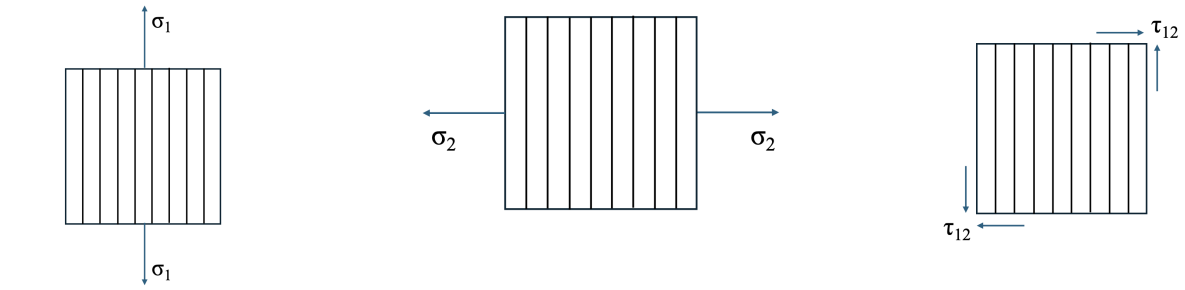

(a) Longitudinal normal. (b) Transverse normal. (c) In-plane shear.

Figure A5: Applied stress states utilized for determining lamina engineering constants.

In the first case, a uniaxial load is applied along the fiber direction, inducing a longitudinal normal stress, σ_1, with all other stresses being zero, as depicted in Figure A5a. In the linear range, empirical observations suggest that the strains along the 1-2 plane can be expressed in terms of engineering constants as follows:

$$\epsilon_1 = \frac{\sigma_1}{E_1} \tag{A16}$$

$$\epsilon_2 = -\nu_{12}\epsilon_1 = -\frac{\nu_{12}\sigma_1}{E_1} \tag{A17}$$

$$\gamma_{12} = 0 \tag{A18}$$

In the second case, when the load is applied perpendicular to the fibers, a transverse normal stress, σ_2, is applied with all other stresses equal to zero, as depicted in Figure A5b. The resulting strains are:

$$\epsilon_2 = \frac{\sigma_2}{E_2} \tag{A19}$$

$$\epsilon_1 = -\nu_{21}\epsilon_2 = -\frac{\nu_{21}\sigma_2}{E_2} \tag{A20}$$

$$\gamma_{12} = 0 \tag{A21}$$

For the third case, a pure shear loading condition along the 1-2 plane ($\sigma_{12} = \tau_{12}$), as shown in Figure A5c, results in:

$$\gamma_{12} = \frac{\tau_{12}}{G_{12}} \tag{A22}$$

$$\epsilon_1 = \epsilon_2 = 0 \tag{A23}$$

where G_{12} represents the shear modulus related to the 1-2 plane.

The empirical observations from Equations A16-A23 can be translated into matrix forms to obtain the reduced stiffness matrices for the orthotropic lamina under plane stress conditions.

Case 1:

$$\begin{Bmatrix} \epsilon_1 \\ \epsilon_2 \\ \gamma_{12} \end{Bmatrix} = \begin{bmatrix} \frac{1}{E_1} & 0 & 0 \\ -\frac{\nu_{12}}{E_1} & 0 & 0 \\ 0 & 0 & 0 \end{bmatrix} \begin{Bmatrix} \sigma_1 \\ \sigma_2 \\ \tau_{12} \end{Bmatrix} \tag{A24}$$

Case 2:

$$\begin{Bmatrix} \epsilon_1 \\ \epsilon_2 \\ \gamma_{12} \end{Bmatrix} = \begin{bmatrix} 0 & -\frac{\nu_{21}}{E_2} & 0 \\ 0 & \frac{1}{E_2} & 0 \\ 0 & 0 & 0 \end{bmatrix} \begin{Bmatrix} \sigma_1 \\ \sigma_2 \\ \tau_{12} \end{Bmatrix} \tag{A25}$$

Case 3:

$$\begin{Bmatrix} \epsilon_1 \\ \epsilon_2 \\ \gamma_{12} \end{Bmatrix} = \begin{bmatrix} 0 & 0 & 0 \\ 0 & 0 & 0 \\ 0 & 0 & \frac{1}{G_{12}} \end{bmatrix} \begin{Bmatrix} \sigma_1 \\ \sigma_2 \\ \tau_{12} \end{Bmatrix} \tag{A26}$$

Utilizing the principle of superposition, valid for linear elastic materials where the stress-strain relationship is linear, the strains calculated independently can be summed to obtain the total strain under a combined loading condition, yielding:

$$\begin{Bmatrix} \epsilon_1 \\ \epsilon_2 \\ \gamma_{12} \end{Bmatrix} = \begin{bmatrix} \frac{1}{E_1} & 0 & 0 \\ \frac{\nu_{12}}{E_1} & 0 & 0 \\ 0 & 0 & 0 \end{bmatrix} \begin{Bmatrix} \sigma_1 \\ \sigma_2 \\ \tau_{12} \end{Bmatrix} + \begin{bmatrix} 0 & \frac{\nu_{21}}{E_2} & 0 \\ 0 & \frac{1}{E_2} & 0 \\ 0 & 0 & 0 \end{bmatrix} \begin{Bmatrix} \sigma_1 \\ \sigma_2 \\ \tau_{12} \end{Bmatrix} + \begin{bmatrix} 0 & 0 & 0 \\ 0 & 0 & 0 \\ 0 & 0 & \frac{1}{G_{12}} \end{bmatrix} \begin{Bmatrix} \sigma_1 \\ \sigma_2 \\ \tau_{12} \end{Bmatrix}$$

which reduces to:

$$\begin{Bmatrix} \epsilon_1 \\ \epsilon_2 \\ \gamma_{12} \end{Bmatrix} = \begin{bmatrix} \frac{1}{E_1} & -\frac{\nu_{21}}{E_2} & 0 \\ -\frac{\nu_{12}}{E_1} & \frac{1}{E_2} & 0 \\ 0 & 0 & \frac{1}{G_{12}} \end{bmatrix} \begin{Bmatrix} \sigma_1 \\ \sigma_2 \\ \tau_{12} \end{Bmatrix} \tag{A27}$$

The relationships between the compliances S_{ij} and the engineering constants can be expressed by the following equations:

$$S_{11} = \frac{1}{E_1}, \quad S_{22} = \frac{1}{E_2}, \quad S_{12} = S_{21} = -\frac{\nu_{21}}{E_2} = -\frac{\nu_{12}}{E_1}, \quad S_{66} = \frac{1}{G_{12}} \tag{A28}$$

Though there are five non-zero values in the compliance matrix, only four of these values are independent. One of the values (either S_{12} or S_{21}) can be expressed as a combination of the other

four independent values, rendering it redundant.

Substituting the coefficients from Equation A28 into Equation A27 results in the original matrix, Equation A15. This matrix serves as a crucial tool in composite material analysis, as it condenses the material's response to various stress states into a concise, two-dimensional representation. It involves condensing the multidirectional elasticity constants to directly relate stress vectors to strain vectors in the lamina's plane.

A.3.2 Deriving the Stress-Strain Relationship in Orthotropic Lamina using Engineering Coefficients

To obtain the stresses in the orthotropic lamina, expressed in tensor strains, from Equation A15, matrix algebra is employed. To isolate the stress vector on the right-hand side, multiply both sides by the inverse of $[S]$, denoted as $[S]^{-1}$:

$$[S^{-1}] \begin{Bmatrix} \epsilon_1 \\ \epsilon_2 \\ \gamma_{12} \end{Bmatrix} = [S^{-1}][S] \begin{Bmatrix} \sigma_1 \\ \sigma_2 \\ \tau_{12} \end{Bmatrix} \tag{A29}$$

Given that $[S][S]^{-1}$ equals the identity matrix $[I]$, where $[I]$ multiplied by any matrix or vector yields the same matrix or vector, this leads to:

$$[S^{-1}] \begin{Bmatrix} \epsilon_1 \\ \epsilon_2 \\ \gamma_{12} \end{Bmatrix} = [I] \begin{Bmatrix} \sigma_1 \\ \sigma_2 \\ \tau_{12} \end{Bmatrix} \tag{A30}$$

Simplifying to:

$$[S^{-1}] \begin{Bmatrix} \epsilon_1 \\ \epsilon_2 \\ \gamma_{12} \end{Bmatrix} = \begin{Bmatrix} \sigma_1 \\ \sigma_2 \\ \tau_{12} \end{Bmatrix} \tag{A31}$$

Hence, the stresses in the 1-2 system can be articulated as follows:

$$\begin{Bmatrix} \sigma_1 \\ \sigma_2 \\ \tau_{12} \end{Bmatrix} = [S^{-1}] \begin{Bmatrix} \epsilon_1 \\ \epsilon_2 \\ \gamma_{12} \end{Bmatrix} \tag{A32}$$

To compute the inverse of $[S]$, the formula for the inverse of a 3×3 matrix is used [98]:

$$S^{-1} = \frac{1}{\det(S)} \cdot \text{adj}(S) \tag{A33}$$

where the determinant is defined as:

$$\det(A) = S_{11}S_{22}S_{66} - S_{12}S_{21}S_{66}$$

The adjugate matrix, adj(S), is derived from the transpose of the cofactor matrix of S. Upon calculating the determinant and the adjugate matrix, the inverse of the matrix is obtained as:

$$S^{-1} = \begin{bmatrix} \frac{S_{22}}{S_{11}S_{22}-S_{12}S_{21}} & -\frac{S_{12}}{S_{11}S_{22}-S_{12}S_{21}} & 0 \\ -\frac{S_{21}}{S_{11}S_{22}-S_{12}S_{21}} & \frac{S_{11}}{S_{11}S_{22}-S_{12}S_{21}} & 0 \\ 0 & 0 & \frac{1}{S_{66}} \end{bmatrix} \tag{A34}$$

Re-expressing Equation A32 by substituting Equation A34 for S^{-1}:

$$\begin{Bmatrix} \sigma_1 \\ \sigma_2 \\ \tau_{12} \end{Bmatrix} = \begin{bmatrix} \frac{S_{22}}{S_{11}S_{22}-S_{12}S_{21}} & -\frac{S_{12}}{S_{11}S_{22}-S_{12}S_{21}} & 0 \\ -\frac{S_{21}}{S_{11}S_{22}-S_{12}S_{21}} & \frac{S_{11}}{S_{11}S_{22}-S_{12}S_{21}} & 0 \\ 0 & 0 & \frac{1}{S_{66}} \end{bmatrix} \begin{Bmatrix} \epsilon_1 \\ \epsilon_2 \\ \gamma_{12} \end{Bmatrix} \tag{A35}$$

Substituting the coefficients from Equation A28 into Equation A34, the values for S_{11}, S_{21}, S_{11}, S_{22}, and S_{66} can be determined, resulting in:

$$\frac{S_{22}}{S_{11}S_{22} - S_{12}^2} = \frac{E_1}{1 - \nu_{12}\nu_{21}} \tag{A36}$$

$$-\frac{S_{12}}{S_{11}S_{22} - S_{12}^2} = \frac{\nu_{12}E_2}{1 - \nu_{12}\nu_{21}} \tag{A37}$$

$$\frac{S_{11}}{S_{11}S_{22} - S_{12}^2} = \frac{E_2}{1 - \nu_{12}\nu_{21}} \tag{A38}$$

$$\frac{1}{S_{66}} = G_{12} \tag{A39}$$

In composite materials analysis, the lamina's stiffness is encapsulated within a matrix called the lamina stiffness matrix, denoted as $[Q]$. This means that the material properties represented in Equations A36 through A39 can be expressed as:

$$Q_{11} = \frac{E_1}{1 - \nu_{12}\nu_{21}}, \quad Q_{12} = Q_{21} = \frac{\nu_{12}E_2}{1 - \nu_{12}\nu_{21}}, \quad Q_{22} = \frac{E_2}{1 - \nu_{12}\nu_{21}} \quad Q_{66} = G_{12} \tag{A40}$$

Reformulating Equation A35 using the Q coefficients from Equation A40:

$$\begin{bmatrix} \sigma_1 \\ \sigma_2 \\ \tau_{12} \end{bmatrix} = \begin{bmatrix} Q_{11} & Q_{12} & 0 \\ Q_{21} & Q_{22} & 0 \\ 0 & 0 & 2Q_{66} \end{bmatrix} \begin{bmatrix} \epsilon_1 \\ \epsilon_2 \\ \gamma_{12}/2 \end{bmatrix} \tag{A41}$$

where the factor of 2 in Q_{66} adjusts for the tensor shear strain, with $\epsilon_{12} = \gamma_{12}/2$.

Equation A41 forms the basis for understanding the mechanical behavior of composites under various loads, representing a transition from the compliance matrix $[S]$ to $[Q]$, shifting focus from deformation response to load-bearing capability by relating the strains in the material to the applied stresses. This approach establishes the Q_{ij} components and connects them to the underlying physical properties described by the engineering constants, clarifying how these quantities are interrelated.

A.3.3 Plane Stress Transformation of Orthotropic Lamina

When analyzing laminates with multiple layers (laminae or plies) bonded together, understanding the stress-strain relationships of orthotropic plies in non-principal coordinates, such as x and y, becomes essential, as depicted in Figure A3. The off-axis stress-strain relationships relate to four independent elastic constants in principal material coordinates and the lamina orientation angle, θ. Figure A6 details the sign convention for θ.

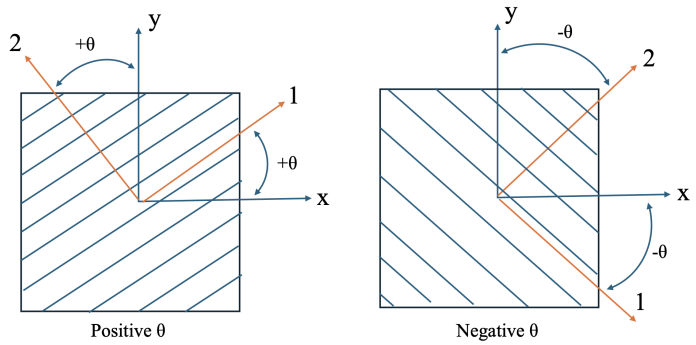

Figure A6: Convention for the sign of lamina orientation.

The equations for transforming stress and strain components from the 1-2 axes to the xy axes are derived by integrating these relationships.

To derive the transformation relationships for stress components between coordinate axes, one can analyze the equations of static equilibrium for a wedge-shaped differential element, as depicted in Figure A7.

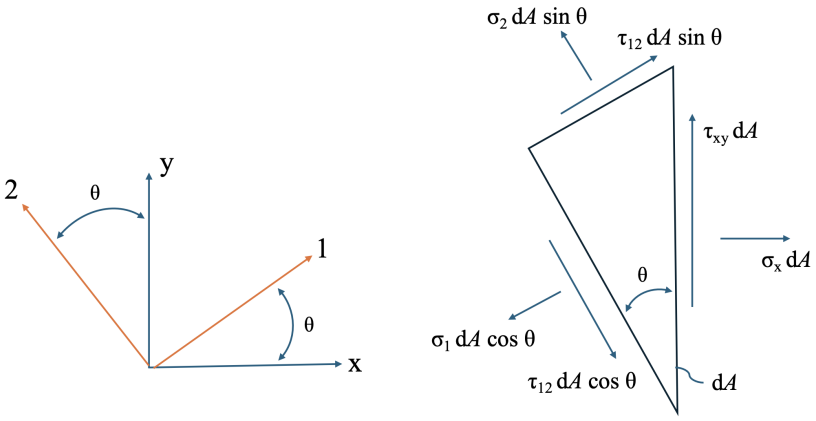

Figure A7: Differential element in static equilibrium with forces in two coordinate systems.

These equilibrium equations provide the required transformation relationships for stress components between coordinate axes. Considering the equilibrium along the x direction:

$$\sum F = \sigma dA - \sigma dA \cos^2\theta - \sigma dA \sin^2\theta + 2\tau dA \sin\theta \cos\theta = 0 \tag{A42}$$

Dividing by dA leads to a relationship between σ_x and the stresses in the 1-2 system:

$$\sigma_x = \sigma_1 \cos^2\theta + \sigma_2 \sin^2\theta - 2\tau_{12} \sin\theta \cos\theta \tag{A43}$$

Applying the same approach yields the complete set of stress transformation equations for the xy-coordinate system in matrix form:

$$\begin{Bmatrix} \sigma_x \\ \sigma_y \\ \tau_{xy} \end{Bmatrix} = \begin{bmatrix} c^2 & s^2 & -2cs \\ s^2 & c^2 & 2cs \\ cs & -cs & c^2 - s^2 \end{bmatrix} \begin{Bmatrix} \sigma_1 \\ \sigma_2 \\ \tau_{12} \end{Bmatrix} = [T]^{-1} \begin{Bmatrix} \sigma_1 \\ \sigma_2 \\ \tau_{12} \end{Bmatrix} \tag{A44}$$

To isolate the vector on the right-hand side, multiply both sides by the inverse of $[T]$, denoted as $[T]^{-1}$:

$$[T] \begin{Bmatrix} \sigma_x \\ \sigma_y \\ \tau_{xy} \end{Bmatrix} = [T][T]^{-1} \begin{Bmatrix} \sigma_1 \\ \sigma_2 \\ \tau_{12} \end{Bmatrix}$$

Since $[T][T]^{-1}$ is the identity matrix, which is denoted as $[I]$, and $[I]$ times any matrix or vector is the matrix or vector itself, therefore:

$$[T] \begin{Bmatrix} \sigma_x \\ \sigma_y \\ \tau_{xy} \end{Bmatrix} = [I] \begin{Bmatrix} \sigma_1 \\ \sigma_2 \\ \tau_{12} \end{Bmatrix}$$

This simplifies to:

$$[T]\begin{Bmatrix}\sigma_x\\ \sigma_y\\ \tau_{xy}\end{Bmatrix}=\begin{Bmatrix}\sigma_1\\ \sigma_2\\ \tau_{12}\end{Bmatrix}$$

Therefore, The stresses in the 1-2 system can be expressed as follows:

$$\begin{Bmatrix}\sigma_1\\ \sigma_2\\ \tau_{12}\end{Bmatrix}=[T]\begin{Bmatrix}\sigma_x\\ \sigma_y\\ \tau_{xy}\end{Bmatrix} \tag{A45}$$

where $c=\cos\theta$ and $s=\sin\theta$. The transformation matrix, $[T]$, facilitates the conversion between the coordinate systems.

It is also demonstrated that tensor strains transform similarly to the stresses, as shown by:

$$[T]=\begin{bmatrix}c^2 & s^2 & 2cs\\ s^2 & c^2 & -2cs\\ -cs & cs & c^2-s^2\end{bmatrix} \tag{A46}$$

It can also be demonstrated that the tensor strains transform in the same manner as the stresses, and that

$$\begin{Bmatrix}\epsilon_1\\ \epsilon_2\\ \frac{\gamma_{12}}{2}\end{Bmatrix}=[T]\begin{Bmatrix}\epsilon_x\\ \epsilon_y\\ \frac{\gamma_{xy}}{2}\end{Bmatrix} \tag{A47}$$

By substituting Equation A47 into Equation A41, and subsequently inserting the resulting equations into Equation A44, it can be determined that

$$\begin{Bmatrix}\sigma_x\\ \sigma_y\\ \tau_{xy}\end{Bmatrix}=[T]^{-1}[Q^*][T]\begin{Bmatrix}\epsilon_x\\ \epsilon_y\\ \frac{\gamma_{xy}}{2}\end{Bmatrix} \tag{A48}$$

The components of the stiffness matrix $[Q^*]$ in Equation A48 are defined as $Q^*_{ij} = Q_{ij}$ for all ij except $Q^*_{66} = 2Q_{66}$. Upon performing the specified matrix multiplications and converting back to engineering strains, it can be obtained that:

$$\begin{Bmatrix} \sigma_x \\ \sigma_y \\ \tau_{xy} \end{Bmatrix} = \begin{bmatrix} \overline{Q}_{11} & \overline{Q}_{12} & \overline{Q}_{16} \\ \overline{Q}_{12} & \overline{Q}_{22} & \overline{Q}_{26} \\ \overline{Q}_{16} & \overline{Q}_{26} & \overline{Q}_{66} \end{bmatrix} \begin{Bmatrix} \epsilon_x \\ \epsilon_y \\ \gamma_{xy} \end{Bmatrix} \tag{A49}$$

where the $\overline{Q}_{ij}$ are the components of the transformed lamina stiffness matrix, which are defined as follows:

$$\begin{aligned}
\overline{Q}_{11} &= Q_{11}c^4 + Q_{22}s^4 + 2(Q_{12} + 2Q_{66})s^2c^2 \\
\overline{Q}_{12} &= (Q_{11} + Q_{22} - 4Q_{66})s^2c^2 + Q_{12}(c^4 + s^4) \\
\overline{Q}_{22} &= Q_{11}s^4 + Q_{22}c^4 + 2(Q_{12} + 2Q_{66})s^2c^2 \\
\overline{Q}_{16} &= (Q_{11} - Q_{12} - 2Q_{66})c^3s - (Q_{22} - Q_{12} - 2Q_{66})cs^3 \\
\overline{Q}_{26} &= (Q_{11} - Q_{12} - 2Q_{66})cs^3 - (Q_{22} - Q_{12} - 2Q_{66})c^3s \\
\overline{Q}_{66} &= (Q_{11} + Q_{22} - 2Q_{12} - 2Q_{66})s^2c^2 + Q_{66}(s^4 + c^4)
\end{aligned}$$

Finally, the transformed orthotropic lamina stiffness matrix (Equation A49) resembles that of an anisotropic material, featuring nine non-zero coefficients. However, only four of these coefficients are independent, as they are expressible in terms of the four independent lamina stiffnesses in plane stress orthotropic conditions. Despite the transformation, the material's orthotropic nature is retained, even though its representation in off-axis coordinates might suggest anisotropy. Experimentally characterizing the lamina in principal material coordinates remains more straightforward than in off-axis coordinates, with the engineering constants (typically measured) directly relating to the lamina stiffnesses as delineated in Equation A40.

Alternatively, the strains can be described in relation to the stresses as:

$$\begin{Bmatrix} \epsilon_x \\ \epsilon_y \\ \gamma_{xy} \end{Bmatrix} = \begin{bmatrix} \tilde{S}_{11} & \tilde{S}_{12} & \tilde{S}_{16} \\ \tilde{S}_{12} & \tilde{S}_{22} & \tilde{S}_{26} \\ \tilde{S}_{16} & \tilde{S}_{26} & \tilde{S}_{66} \end{bmatrix} \begin{Bmatrix} \sigma_x \\ \sigma_y \\ \tau_{xy} \end{Bmatrix} \tag{A50}$$

where the $\overline{S}_{ij}$ are the components of the transformed lamina compliance matrix, defined by $[S] = [Q]^{-1}$:

$$\begin{aligned}
\overline{S}_{11} &= S_{11}c^4 + (2S_{12} + S_{66})s^2c^2 + S_{22}s^4 \\
\overline{S}_{12} &= S_{12}(s^4 + c^4) + (S_{11} + S_{22} - S_{66})s^2c^2 \\
\overline{S}_{22} &= S_{11}s^4 + (2S_{12} + S_{66})s^2c^2 + S_{22}c^4 \\
\overline{S}_{16} &= (2S_{11} - 2S_{12} - S_{66})s^3c - (2S_{22} - 2S_{12} - S_{66})s^3c \\
\overline{S}_{26} &= (2S_{11} - 2S_{12} - S_{66})s^3c - (2S_{22} - 2S_{12} - S_{66})s^3c \\
\overline{S}_{66} &= 2(2S_{11} + 2S_{22} - 4S_{12} - S_{66})s^2c^2 + S_{66}(s^4 + c^4)
\end{aligned}$$

Appendix B. MATLAB Codes

B.1 Mesh Convergence

```
1
2
3  %% Convergence plots
4
5  clear
6  clc
7  close all
8  warning ('off','all');
9
10 % Load the data
11 data = readtable('output_file.csv');
12
13 % Filter data for each category
14 c2_data = data(contains(data.ModelType, 'C2'), :);
15
16 % Plotting
17 lw = 2;
18 ms = 13;
19 fs = 13;
20
21 figure;
22 plot(c2_data.NumberOfElements, c2_data.CriticalBucklingLoadEigenvalue_N_/1000,
       'v-','LineWidth', lw,'MarkerSize', ms,'MarkerFaceColor','#EDB120');
23 %title('C2 Buckling Values');
24 xlabel('Number of Elements');
25 ylabel('Critical Buckling Load Eigenvalue [kN]');
26 set(gca,'FontSize',fs)
27 grid on
28 print(gcf, 'C2_Buckling_Plot.png', '-dpng', '-r1200');
29
30 %% Convergence Table
31
32 clear
33 clc
34 close all
35 warning ('off','all');
36
```

```
% Load the CSV data
data = readtable('output_file.csv');

% Extract the 'C' category from the 'ModelType' string
data.C_Category = regexprep(data.ModelType, '(C\d+)/.*', '$1');

% Filter data for the 'C2' category
c_data = data(strcmp(data.C_Category, 'C2'), :);

% Sort by number of elements (assuming more elements means finer mesh)
c_data = sortrows(c_data, 'NumberOfElements', 'descend');

% Experimental Buckling loads [N] for 'C2'
experimental_eigenvalue = 30117;  % Example value for C2, adjust as necessary

% Calculate the percentage error with respect to the experimental eigenvalue
percentage_errors = abs((c_data.('CriticalBucklingLoadEigenvalue_N_') -
    experimental_eigenvalue) ./ experimental_eigenvalue) * 100;

% Create a table for 'C2'
convergence_table = table(c_data.NumberOfElements, ...
                          c_data.('CriticalBucklingLoadEigenvalue_N_'), ...
                          percentage_errors, ...
                          'VariableNames', {'Number_of_Elements', 'Eigenvalue',
                              'Percentage_Error'});

% Write the table to a CSV file for the 'C2' category
csv_filename = 'C2_convergence.csv';
writetable(convergence_table, csv_filename);

disp('CSV files for each C category created successfully.');
```

Listing 1: meshconvergence.m

B.2 Data Processing for C2 C-beam

```
% MATLAB Script to plot arc length vs LPF for configuration C2

close all;
clc;
clear all;
```

```
6
7  % Define filename for C2
8  file = 'C2_LPF_ArcLength.xlsx';
9  label = 'C2';
10
11 % Prepare the plot
12 figure;
13 hold on; % Hold on to plot
14
15 % Define line style
16 lineStyle = '-';
17 color = [0 0.4470 0.7410]; % Typical blue color
18
19 % Read data from file
20 data = readtable(file, 'Range', 'A2:B100'); % Adjust the range as needed
21 arc_length = data.Var1;
22 ldp = data.Var2;
23
24 % Plot data
25 plot(arc_length, ldp, 'LineWidth', 3, 'LineStyle', lineStyle, 'Color', color);
26
27 % Add labels, legend, and grid
28 % Set font size
29 ax = gca; % Get current axes
30 ax.FontSize = 14; % Set font size for axes labels and tick labels
31 xlabel('Arc Length [-]', 'FontSize', 14); % Set font size for x-axis label
32 ylabel('Load Proportionality Factor (LPF) [-]', 'FontSize', 14); % Set font size for
       y-axis label
33 %legend(label, 'FontSize', 15, 'Location', 'southeast'); % Set font size for legend
34 grid on;
35 hold off;
36
37 % Save the figure
38 filename = 'C2_ArcLength_vs_LPF.png'; % Define the filename and format
39 print('-dpng', '-r1200', filename); % Save as PNG at 1200 DPI
```

Listing 2: C2NonLinearLPF.m

B.3 Data Processing for C1-C5 C-beam

```
1  % MATLAB Script to plot arc length vs LPF for multiple configurations
```

```
2
3  close all
4  clc
5  clear all
6
7  % Define filenames
8  files = {'C1_LPF_ArcLength.xlsx', 'C2_LPF_ArcLength.xlsx', 'C3_LPF_ArcLength.xlsx', ...
9           'C4_LPF_ArcLength.xlsx', 'C5_LPF_ArcLength.xlsx'};
10 labels = {'C1', 'C2', 'C3', 'C4', 'C5'};
11
12 % Prepare the plot
13 figure;
14 hold on; % Hold on to plot multiple lines
15
16 % Define line styles
17 lineStyles = {'-', '--', '-', '-.', ':'};
18 colors = lines(numel(files)); % Get distinct colors
19
20 % Loop through files and plot with different line styles
21 for i = 1:length(files)
22     data = readtable(files{i}, 'Range', 'A2:B100'); % Adjust the range as needed
23     arc_length = data.Var1;
24     ldp = data.Var2;
25
26     % Plot data with different line styles and colors
27     plot(arc_length, ldp, 'LineWidth', 3, 'LineStyle', lineStyles{i}, 'Color',
           colors(i,:));
28 end
29
30 % Add labels, legend, and grid
31 % Set font size
32 ax = gca; % Get current axes
33 ax.FontSize = 14; % Set font size for axes labels and tick labels
34 xlabel('Arc Length [-]', 'FontSize', 14); % Set font size for x-axis label
35 ylabel('Load Proportionality Factor (LPF) [-]', 'FontSize', 14); % Set font size for
       y-axis label
36 legend(labels, 'FontSize', 15, 'Location', 'southeast'); % Set font size for legend
37 grid on;
38 hold off;
39
40 % Save the figure
```

```
filename = 'ArcLength_vs_LPF.png'; % Define the filename and format
print('-dpng', '-r1200', filename); % Save as PNG at 1200 DPI
```

Listing 3: NonLinearLPF.m

B.4 Data Processing for Cross C2 C-beam

```
% MATLAB Script to plot arc length vs LPF for None and Cross configurations

close all
clc
clear all

% Define filenames
files = {'C2_LPF_ArcLength.xlsx', 'Cross_LPF_ArcLength.xlsx'};
labels = {'No Stiffener', 'Cross Stiffener'};

% Prepare the plot
figure;
hold on; % Hold on to plot multiple lines

% Define line styles
lineStyles = {'-', '-.'};
colors = lines(numel(files)); % Get distinct colors

% Loop through files and plot with different line styles
for i = 1:length(files)
    data = readtable(files{i}, 'Range', 'A2:B100'); % Adjust the range as needed
    arc_length = data.Var1;
    ldp = data.Var2;

    % Plot data with different line styles and colors
    plot(arc_length, ldp, 'LineWidth', 3, 'LineStyle', lineStyles{i}, 'Color',
        colors(i,:));
end

% Add labels, legend, and grid
% Set font size
ax = gca; % Get current axes
ax.FontSize = 14; % Set font size for axes labels and tick labels
xlabel('Arc Length [-]', 'FontSize', 14); % Set font size for x-axis label
```

```
ylabel('Load Proportionality Factor (LPF) [-]', 'FontSize', 14); % Set font size for
    y-axis label
legend(labels, 'FontSize', 15, 'Location', 'southeast'); % Set font size for legend
grid on;
hold off;

% Save the figure
filename = 'ArcLength_vs_LPF_Cross.png'; % Define the filename and format
print('-dpng', '-r1200', filename); % Save as PNG at 1200 DPI
```

Listing 4: CrossNonLinearLPF.m

B.5 Data Processing for Cross C2 C-beam Axial Loads

```
% MATLAB Script to plot arc length vs LPF for None and Cross configurations

close all
clc
clear all

% Define filenames
files = {'C2_LPF_ArcLength.xlsx', 'Cross_LPF_ArcLength.xlsx'};
labels = {'No Stiffener', 'Cross Stiffener'};

% Prepare the plot
figure;
hold on; % Hold on to plot multiple lines

% Define line styles
lineStyles = {'-', '-.'};
colors = lines(numel(files)); % Get distinct colors

% Loop through files and plot with different line styles
for i = 1:length(files)
    data = readtable(files{i}, 'Range', 'A2:B100'); % Adjust the range as needed
    arc_length = data.Var1;
    ldp = data.Var2;
    if i == 1
        ldp = 28.015*ldp;
    else
        ldp = 32.070*ldp;
```

```
    end

    % Plot data with different line styles and colors
    plot(arc_length, ldp, 'LineWidth', 3, 'LineStyle', lineStyles{i}, 'Color',
        colors(i,:));
end

% Add labels, legend, and grid
% Set font size
ax = gca; % Get current axes
ax.FontSize = 14; % Set font size for axes labels and tick labels
xlabel('Arc Length [-]', 'FontSize', 14); % Set font size for x-axis label
ylabel('Axial Load [kN]', 'FontSize', 14); % Set font size for y-axis label
legend(labels, 'FontSize', 15, 'Location', 'southeast'); % Set font size for legend
grid on;
hold off;

% Save the figure
filename = 'ArcLength_vs_AxialLoad_Cross.png'; % Define the filename and format
print('-dpng', '-r1200', filename); % Save as PNG at 1200 DPI
```

Listing 5: CrossNonLinearLoads.m

Appendix C. CSV files

C.1 Load proportionality factor (LPF) vs arc length for C2 C-beam

arc length	**LPF**
0.01	0.010000193
0.02	0.020000767
0.035	0.035002336
0.057500001	0.057506245
0.091250002	0.091265485
0.141874999	0.141911447
0.217812493	0.217894092
0.331718743	0.331887007
0.502578139	0.502829432
0.758867204	0.757612169
1.143300772	1.051570296

arc length	LPF
1.335517526	1.054296613
1.479680181	1.058781028
1.695924044	1.068521261
2.020289898	1.089539886
2.506838799	1.132440329
3.236661911	1.213580966
4.33139658	1.353793144
4.605080128	1.380905747
4.878764153	1.403043866
5.289289474	1.413064957
5.699814796	1.426363111
6.110340595	1.44183135
6.726128578	1.458318472
7.341917038	1.460662484
7.957705498	1.462522864
8.881387711	1.46661365
10.26691151	1.47028935
11.6524353	1.481140137
13.0379591	1.496285915
14.42348194	1.512672901
15.80900574	1.52858758
17.19453049	1.54331255
19.2728157	1.561989546
22.39024353	1.583345056
25.50767136	1.596986294
28.62509918	1.601467609
31.74252701	1.593406081

C.2 Load proportionality factor (LPF) vs arc length for C1 C-beam

arc length	**LPF**
0.01	0.010000193
0.02	0.020000767
0.035	0.035002336
0.057500001	0.057506237
0.091250002	0.091265447
0.141874999	0.141911298
0.217812493	0.217893451
0.331718743	0.331883907
0.502578139	0.502810299
0.758867204	0.757330894
0.854975581	0.883220255

arc length	LPF
1.215382099	0.987199843
1.539747953	1.019696355
2.026296616	1.075608492
2.756119728	1.186361194
3.029803514	1.257095695
3.098224401	1.259614348
3.166645288	1.258373499
3.269276857	1.252648115
3.423223734	1.241409063
3.654144526	1.22398448
4.000525475	1.245562315
4.346906185	1.302427888
4.693287373	1.360006928
5.039668083	1.39886117
5.559239388	1.433472991
6.338596344	1.454608321
7.507632256	1.467728496
8.676667213	1.481131911
9.845703125	1.491477847
11.01473904	1.498408198
12.18377399	1.501520872
13.35280991	1.500556111
14.52184582	1.495892048
16.27539825	1.481897712
18.02895164	1.461540103

C.3 Load proportionality factor (LPF) vs arc length for C3 C-beam

arc length	**LPF**
0.01	0.01000019
0.02	0.020000754
0.035	0.035002295
0.057500001	0.057506133
0.091250002	0.091265194
0.141874999	0.141910702
0.217812493	0.217892215
0.331718743	0.331882238
0.502578139	0.502817452
0.758867204	0.757555604
1.143300772	1.042741895

arc length	LPF
1.912168026	1.087486863
2.296601534	1.120255828
2.39270997	1.130259514
2.536872625	1.145898223
2.753116369	1.171226144
3.077482224	1.215316176
3.564031124	1.331942201
4.050580025	1.385818481
4.537128448	1.42620039
5.023677349	1.42689538
5.51022625	1.427105904
5.996774673	1.428581476
6.726598263	1.431319833
7.821332932	1.432298779
9.463435173	1.434600949
11.10553741	1.442970872
12.7476387	1.453373313
14.38974094	1.463305354
16.03184319	1.471740723
17.67394447	1.478381634
20.13709831	1.484372497
23.83182907	1.485443473
27.52655792	1.478344321
31.22128677	1.462625623

C.4 Load proportionality factor (LPF) vs arc length for C4 C-beam

arc length	**LPF**
0.01	0.01000018
0.02	0.020000719
0.035	0.035002183
0.057500001	0.057505824
0.091250002	0.091264397
0.141874999	0.141908705
0.217812493	0.217887238
0.331718743	0.331869215
0.502578139	0.502777934
0.758867204	0.757329941
0.854975581	0.883763731

arc length	LPF
1.215382099	0.987213135
1.539747953	1.019383669
2.026296616	1.074977756
2.756119728	1.185393691
3.029803514	1.258574367
3.132434845	1.288733125
3.235066175	1.289285302
3.337697744	1.281148553
3.440329075	1.271892071
3.59427619	1.262833357
3.825196743	1.278157234
4.171577454	1.338013887
4.517958641	1.399929404
4.864339352	1.433814287
5.210720539	1.448833823
5.730291843	1.45776403
6.5096488	1.468830824
7.289005756	1.478663564
8.06836319	1.484001279
8.847720146	1.485172391
9.627077103	1.481926322
10.40643406	1.474554062

C.5 Load proportionality factor (LPF) vs arc length for C5 C-beam

arc length	**LPF**
0.01	0.01000013
0.02	0.020000514
0.035	0.035001554
0.057500001	0.057504106
0.091250002	0.091259979
0.141874999	0.141897634
0.217812493	0.217859417
0.331718743	0.331795901
0.502578139	0.502549708
0.758867204	0.755939305
0.854975581	0.877039015

arc length	LPF
1.215382099	0.980432928
1.539747953	1.011039257
2.026296616	1.060123444
2.756119728	1.155091524
3.850854635	1.337489247
4.124538422	1.36561811
4.39822197	1.364126205
4.671905518	1.353507519
5.082431316	1.33455348
5.698219299	1.340125203
6.314007759	1.39732337
6.929796219	1.461386919
7.853478432	1.535093904
9.239002228	1.588363528
10.62452602	1.609601736
12.01004887	1.624408126
14.08833504	1.637017965
16.16662025	1.644220471
18.24490547	1.645344615
20.32319069	1.64050436
22.40147591	1.629628658
24.47976112	1.613476157

C.6 Load proportionality factor (LPF) vs arc length for Cross Stiffener C2 C-beam

arc length	**LPF**
0.01	0.010001337
0.02	0.020005383
0.035	0.035016757
0.057500001	0.057546362
0.091250002	0.091371126
0.141874999	0.142183959
0.217812493	0.218598485
0.331718743	0.333729565
0.502578139	0.507395506
0.758867204	0.754854918
1.143300772	0.908366323

arc length	LPF
2.584926844	1.094468713
3.882390022	1.241264939
5.179853439	1.31898284
6.477316856	1.369721174
7.774780273	1.405649185
9.07224369	1.426942468
10.36970711	1.446128249
12.31590176	1.468038321
14.26209736	1.486974478
14.74864578	1.49222219
15.23519516	1.49678719
15.72174358	1.500997782
16.4515667	1.506694794
17.54630089	1.514090538
19.18840408	1.523249149
21.65155602	1.532988787
25.34628677	1.537303448
29.04101563	1.530619025
32.73574448	1.515411258
36.43047714	1.493813396